Limestone calcination nearby equilibrium: Kinetics, CaO crystal structure, sintering and reactivity

J. M. Valverde[a], P. E. Sanchez-Jimenez[b], L. A. Perez-Maqueda[b]

[a] Faculty of Physics. University of Seville. Avenida Reina Mercedes s/n, 41012 Sevilla, Spain

[b] Instituto de Ciencia de Materiales de Sevilla (C.S.I.C.-Univ. Seville), Americo Vespucio 49, 41092 Sevilla, Spain

Abstract

In this work we analyze limestone calcination at environmental conditions involving a CO_2 partial pressure P close to the equilibrium pressure P_{eq} by means of in-situ X-ray diffraction (XRD) and thermogravimetric (TG) analyses. In contrast with previous empirical observations carried out mostly at conditions far from equilibrium ($P/P_{eq} << 1$), our results show that the decarbonation rate decreases as the temperature in increased while P/P_{eq} is kept constant, which is explained from a reaction mechanism including desorption and the exothermic structural transformation from metastable CaO^* nanocrystals to the stable CaO form. The crystal structure and sintering of nascent CaO during calcination has been investigated from in-situ XRD analysis, physisorption analysis and Scanning Electron Microscopy (SEM), which shows that the ratio of the size of polycrystalline CaO grains to crystallite size increases linearly with the CO_2 partial pressure in the calcination atmosphere. For high CO_2 partial pressures, the size of CaO grains reaches a maximum value of around 1 μm, which leads to a residual surface area of about 1 m^2/g, whereas in the limit $P \to 0$ grain size and crystallite size (of the order of 10 nm) would coincide. Accordingly, sintering in the presence of CO_2 would be triggered by the agglomeration of CaO crystals enhanced by CO_2 adsorption, which increases the surface energy. The carbonation reactivity of CaO resulting from calcination scales proportionally to its surface area and is not determined by a growth of the CaO exposed surface along a preferred crystallographic direction wherein carbonation would be unfavorable as suggested in recent works.

I. INTRODUCTION

The endothermic decomposition of limestone ($CaCO_3$)

$$CaCO_3 \leftrightarrows CaO + CO_2 \quad \Delta_r H^0 = +177.8\text{kJ/mol} \tag{1}$$

is at the heart of a myriad of industrial and natural processes (see [1] and references therein). Lime (CaO) is a main ingredient of technologies employed in a wide variety of industries such as construction, agriculture, food processing, disinfection, water treatment, SO_2 post-combustion capture, steel-making, plastics and glass, and sugar refining. Nowadays, the number of applications wherein this apparently simple decomposition reaction plays a central role continues to add on. The Ca-looping (CaL) technology, which is built on the multicyclic calcination/carbonation of limestone, has recently emerged as a feasible process for CO_2 capture from industrial concentrated sources such as coal combustion plants [2–4]. The CaL technology is being currently investigated as a method to store and controllably dispatch thermal energy in concentrated solar power plants (CSP) [5] as early proposed in the 1980s [6]. The wide availability, low cost and harmlessness towards the environment of natural limestone would contribute to boost the competitiveness of these processes to reach a commercial level. Nevertheless, a number of issues might still hamper their large scale development such as the marked deceleration of decomposition when calcination is carried out under high CO_2 partial pressure and high temperature as required in post-combustion CO_2 capture and the poor carbonation reactivity of CaO resulting from decomposition at these conditions [7, 8]. Certainly, a fundamental understanding of the physic-chemical processes that govern the thermal decomposition of $CaCO_3$ would be of paramount importance in order to devise strategies for improving the efficiency of technical applications in which this reaction is involved.

A vast number of studies may be found in the literature with the goal of getting a grip on the driving mechanisms behind the $CaCO_3$ thermal decomposition [1, 9–19]. Most of them analyze the reaction kinetics as affected by the calcination temperature T and the $CaCO_3$ conversion degree α (ratio of mass of $CaCO_3$ decarbonated to initial mass). The conversion rate is commonly measured by means of thermogravimetric analysis (TGA) and can be in general well fitted by the widely accepted Arrhenius type law

$$\frac{d\alpha}{dt} = A\, f(\alpha)\, \exp(-E/RT) \left(1 - \frac{P}{P_{eq}}\right)^{\gamma} \tag{2}$$

where A is a pre-exponential term, $\gamma \sim 1$, $E > 0$ is the so-called activation energy, $R = 8.3145$ J/mol-K is the ideal gas constant, P is the CO_2 partial pressure and P_{eq} is the CO_2 partial pressure for the reaction to be at equilibrium, which is given by

$$P_{eq}(\mathrm{atm}) \approx 4.083 \times 10^{7} \exp(-20474/T) \tag{3}$$

as inferred from thermochemical empirical data [17, 20, 21]. Even though Eq. 2 is widely accepted, the Arrehnius equation for solid-state reactions is hardly justifiable from purely theoretical grounds since the Maxwell–Boltzmann equation on which it is based is only applicable to the energy distribution of molecules in an ideal gas and not to the immobilized ions of a crystalline reactant [19, 22]. Moreover, the decarbonation process generally consists of several steps such as chemical decomposition, structural transformation and physical desorption.

A number of functional forms $f(\alpha)$ have been proposed to account for the influence on the reaction progress of diverse mechanisms such as nucleation and growth, impeded CO_2 diffusion or geometrical constraints related to particles' shape and pore size distribution of the powder [23], whose relative importance generally depends on the particular conditions of calcination [16]. In regards to the pressure term in the right hand side of Eq. 2, it is often neglected since experimental conditions usually imply $P << P_{eq}$ [1, 9, 11–13, 15–17, 19, 24]. Under these conditions, chemical decomposition is supposed to be the only relevant step of the reaction and the conversion rate is generally well fitted in a broad rage of conversion by the product of the mechanistic-rate function $f(\alpha)$ and an Arrhenius law with apparent activation energies around the reaction enthalpy change, mainly between 100 and 230 kJ/mol [22]. However, the widely spread range of activation energies found experimentally, which is also observed for decomposition of single calcite crystals [1, 24], suggests that the reaction rate is not exclusively determined by chemical decomposition [19, 24]. The apparent activation energy in Eq. 2 should be interpreted in terms of the activation energies and enthalpy variations of the preponderant mechanisms which may in turn be a function of the degree of conversion α [19]. On the other hand, experimental evidences indicate [1, 24] that decomposition of calcite yields a metastable solid phase product whose transformation into the stable CaO is exothermic [18, 25] although it is seen to occur very fast in the limit $P/P_{eq} << 1$ to have any possible influence on the reaction rate [1].

In the study on limestone decomposition reported in the present manuscript, the approach adopted was motivated by the calcination conditions in the recently emerged Ca-looping technology for post-combustion CO_2 capture. In this novel application, the CO_2 sorbent (CaO) has to be regenerated in a fluidized bed reactor (calciner) operated at atmospheric pressure and where the partial pressure of CO_2 must be necessarily high (between 70 and 90 kPa) in order to retrieve from it a stream of CO_2 at high concentration to be compressed, transported and stored. Therefore, calcination temperatures have to be rather high (typically above 900°C) in order to shift the reaction equilibrium towards decarbonation. Moreover, full decarbonation has to be achieved in typically short residence times (on the order of minutes) due to technological constraints, which demands increasing even further the calcination temperature to values close to 950°C. This imposes an important energy penalty and hinders the industrial competitiveness of the technology [26–29]. A further issue is that the CaO stemming from calcination at high CO_2 partial pressure and high temperature has a significantly low carbonation reactivity [7, 8]. Diverse strategies have been devised aimed at decreasing the calcination temperature such as using low crystalline limestone or dolomite, which exhibit a faster decomposition at high CO_2 partial pressure [8, 30].

In our work, we have investigated limestone decarbonation at CO_2 partial pressure and temperature conditions nearby equilibrium ($P/P_{eq} \lesssim 1$). To this end calcination tests have been carried out in a broad range of temperatures and for CO_2 partial pressures close to the equilibrium pressure. TGA tests were complemented with in-situ X-ray diffraction (XRD) analysis allowing us to investigate the time evolution of CaO crystal structure during decarbonation. A further subject that has been studied is the sintering and carbonation reactivity of CaO derived from calcination at conditions nearby equilibrium. In-situ XRD and SEM analyses served to look at the quantitative correlation between the reduction of surface area due to sintering and CaO reactivity as determined by the calcination conditions. The in-situ XRD analysis helped us extracting information also on the linkage between the transformation mechanism, CaO crystal size enlargement and sintering. Moreover, it allowed us investigating whether the very low reactivity of CaO resulting from calcination at high temperature and high CO_2 pressure might be caused by a preferential orientation of the CaO surface along poorly reactive (200) crystallographic planes (on which CO_2 chemisorption is energetically unfavorable at high temperature [31–33]) and not merely due to the reduction of CaO surface area by sintering.

II. MATERIALS AND METHODS

The limestone tested in our work has been a natural limestone from Matagallar quarry (Pedrera, Spain) of high purity (99.62% $CaCO_3$, $SiO_2 < 0.05\%$, $Al_2O_3 < 0.05\%$, 0.24% MgO, 0.08% Na_2O) and a small particle size (9.5 μm volume weighted mean particle size)

X-ray diffraction (XRD) analysis was performed using a Bruker D8 Advance powder diffractometer equipped with a high temperature chamber (Anton Paar XRK 900) and a fast response/high sensitivity detector (Bruker Vantec 1) allowing us to look at the time evolution of the crystal structure in-situ as calcination progresses. A sufficiently large number of counts is retrieved by means of 140 s duration XRD scans continuously recorded in the range $2\theta \in (27.5^\circ, 39.5^\circ)$ (0.022°/step) wherein the main Bragg reflection peaks for calcite and lime are located. Since the interaction volume of the Cu K-alpha radiation (0.15405 nm wavelength) employed in the equipment with the sample typically comprises a depth of up to 100μm, which is much larger than particle size, the diffractograms obtained are useful to reliably estimate the $CaCO_3$/CaO weight fraction during in-situ calcination by means of a semi-quantitative analysis. In this setup, the limestone sample is held on a 1 cm diameter porous ceramic plate through which a N_2/CO_2 mixture (with controlled CO_2 vol.%) is passed at a small flow rate (100 $cm^3 min^{-1}$) and atmospheric pressure. The temperature is increased from ambient temperature at 12°C/min up to the target calcination temperature, which is kept constant for about 1 h while XRD scans are continuously registered.

The kinetics of limestone decomposition was also investigated in our work by means of TGA at the same conditions as those employed in the XRD analysis. TGA tests were carried out using a Q5000IR TG analyzer (TA Instruments). This instrument is provided with an infrared furnace heated by halogen lamps and a high sensitivity balance (<0.1 μg) characterized by a minimum baseline dynamic drift (<10 μg). TGA was also employed to measure the carbonation reactivity of CaO resulting form calcination, which was accomplished by quickly decreasing the temperature down to 650°C (300°C/min rate) and subjecting the sample to a gas mixture of 85% dry air/15% CO_2 vol/vol (typical of post-combustion flue gas) for 5 min.

In order to obtain reliable kinetic data from both XRD and TGA tests it is of great importance to minimize mass and heat transfer phenomena that might influence the reaction rate uncontrollably. As noted in previous works on the kinetics of limestone decomposition based on TGA, undesired effects due to diffusion resistance through the sample become relevant in this type of analysis for sample masses above ∼40 mg [16]. Mass transfer phenomena can be neglected for sample masses of 10 mg as used in our tests. On the other hand, in-situ XRD calcination tests require the use of sample masses of around 150 mg. However, the gas-solid contacting efficiency in this setup is favored and mass transfer phenomena minimized since the gas is passed directly through the sample layer whereas in the TG analyzer the gas flows over it. The XRK 900 reactor chamber employed in our in-situ XRD tests is specifically designed for the kinetic analysis of gas-solid reactions up to 900°C. The entire set of sample and sample holder is placed inside a furnace with a heater that guarantees temperature uniformity and the absence of temperature gradients in the sample. NiCr/NiAl thermocouples are positioned inside the furnace and on the ceramic sample holder providing a reliable measurement and control of the sample temperature. As regards the TG analyzer, heat transfer phenomena are minimizing by positioning the sample inside a SiC enclosure that is heated with four symmetrically placed IR lamps ensuring consistent and uniform heating. Moreover, active water-cooling of the surrounding furnace body provides an efficient heat-sink and facilitates precise temperature and rate control. The temperature is registered by a thermocouple positioned close to the sample underneath it. Quick heating of the gas up to the desired temperature is achieved by using a small gas flow rate in both experiments (100 $\mathrm{cm^3 min^{-1}}$). At this small flow rate the gas velocity has no influence on the reaction rate [34]. In both setups the sample chamber is specially designed without any dead volumes to ensure homogeneous filling with the reaction gas. Finally, concerning particle size intra-particle diffusion resistance may play a role on the reaction rate for particles of size larger than 300 μm [17, 35], which is much larger than the average size of the particles in our samples.

Scanning Electron Microscopy (SEM) analysis was made by means of a HITACHI Ultra High-Resolution S-5200 on the calcined samples in the XRD tests, which were also subjected to physisorption analysis using a TriStar II 3020 V1.03 analyzer operated by N_2 sorption at 77 K. Additional physisorption analysis was carried out using Kr at 77 K as adsorbate whose small vapor pressure allows measuring very small adsorptions with reasonable precision, which resulted more convenient for CaO samples with quite low specific surfaces derived from calcination at severe conditions (high temperature and high CO_2 vol%).

Values of CO_2 partial pressure (P (kPa) $\simeq$ CO_2 vol.% at atmospheric pressure) and temperature T for which limestone decarbonation has been investigated in our tests are plotted in Fig. 1 along with the equilibrium CO_2 partial pressure P_{eq} vs. T curve (Eq. 3). Values of P/P_{eq} (between 0.6 and 0.85) are shown in the inset as a function of calcination temperature indicating whether decarbonation was complete, partial or not even initiated in the 60 min calcination period of the in-situ XRD tests. A first remarkable observation is that, for a given value of P/P_{eq}, there is an important effect of temperature on the rate of decarbonation in the opposed sense indicated by Eq. 2. For example, for $P/P_{eq} \simeq 0.85$, decarbonation is completed in just about 20 min at 790°C (15% CO_2) whereas it is not finished in the 60 min calcination period at 860°C (50% CO_2) and at 880°C (70% CO_2) decarbonation is not even started. Thus, if P/P_{eq} is kept constant, decarbonation is hindered as the temperature is increased.

III. IN-SITU XRD ANALYSIS

Figure 2 shows an example of the diffractograms continuously retrieved during an in-situ XRD calcination test. Since each scan takes only 140 s, which is much smaller than the typical decarbonation time, the analysis of these diffractograms allows us carrying out an study on the reaction kinetics and the accompanying structural change. The ratio between intensities of Bragg main reflection peaks for $CaCO_3$ (I_{211}) and CaO (I_{200}) is plotted in Fig. 5 as a function of the calcination time. As already pointed out, a main feature of the results is that, for similar values of P/P_{eq}, the reaction becomes substantially slower as the temperature is increased. A remarkable behavior is seen for calcination at 890°C under 70%CO_2 (P/P_{eq}=0.76). Under these conditions, the $CaCO_3$ peak intensity remains around its highest value for a long induction period of about 30 min at the calcination temperature after which it starts to decrease very slowly. Calcination at 860°/50% CO_2 shows also a noticeable induction period, although shorter, after the calcination temperature is reached. In general, it is seen that decarbonation starts sooner and becomes quicker as the CO_2 vol.% and temperature are decreased while P/P_{eq} is kept constant.

Taking into account the corundum numbers for calcite ($k_c = I'_{211}/I_{cor}$=3.48 for a 50:50 wt.% mixture of calcite with corundum) and lime ($k_l = I'_{200}/I_{cor}$=4.85 for a 50:50 wt.% mixture of lime with corundum), the reference intensity ratio method usually employed in XRD analysis may be used to estimate the time evolution of the $CaCO_3$/CaO weight fraction from the measured Bragg peaks intensities ($m_{CaCO3}/m_{CaO} \approx (k_l/k_c)I_{211}/I_{200} = 1.39 I_{211}/I_{200}$). As observed in Fig. 5, the ratio I_{211}/I_{200} fits satisfactorily to an exponential decay with time once decarbonation is initiated. Thus, $CaCO_3$ conversion (α defined as the ratio of mass $CaCO_3$ decarbonated to initial mass) is given by $(1-\alpha)/\alpha = 1.39\,(M_{CaCO3}/M_{CaO})(I_{211}/I_{200}) \propto \exp(-\beta t)$, where $M_{CaCO3}/M_{CaO} = 100/56$ is the ratio of molecular weights and t is time. Taking the time derivative it is readily obtained

$$\frac{d\alpha}{dt} = f(\alpha)\beta(T, P) \tag{4}$$

where $f(\alpha) = \alpha(1-\alpha)$, which is consistent with the Prout-Tompkins mechanistic rate-equation. Accordingly, decarbonation would be initiated after an induction period at nucleation sites with enhanced local reactivity such as surface structural defects. The reaction would be then auto-catalyzed and accelerated as decarbonation progresses finishing with a deceleration period [23, 36]. The existence of an induction period for decarbonation of calcite crystals to be started in CO_2 enriched atmospheres was already observed by Hyatt et al. [9].

Assuming that the reaction is initiated at specific reactive sites near the crystal's structural imperfections, an increase of the density of defects and dislocations by pretreatment would serve to enhance nucleation. Results reported elsewhere [8] showing that pretreatment by ball milling enhances decarbonation at high temperature nearby equilibrium are consistent with this picture.

Equation 4 indicates that the dependence of the reaction rate (for a given value of conversion α) on CO_2 partial pressure P and temperature T at the conditions close to equilibrium of our experiments may be expressed separately by the function $\beta(T, P)$, which does not conform to the widely accepted Arrhenius law with a positive activation energy (Eq. 2).

Contrarily, we see that, for a given value of P/P_{eq}, β is a decreasing function of temperature. As will be analyzed in detail below (section V), this peculiar dependence on temperature can be explained by means of a reaction mechanism consisting not just of chemical decomposition but also CO_2 desorption and an exothermic transformation of CaO structure to its final stable form. Arguably, the exothermicity of CaO structural transformation might contribute to the auto-catalytic effect inferred from the dependence of the conversion rate on α.

Let us now focus on the analysis of the time evolution of CaO crystal structure during decarbonation. The diffractograms obtained during decarbonation are useful to address the question on a possible preferential growth of the CaO crystal structure along poorly reactive (200) planes, which has been suggested in recent theoretical works as a cause of its very low reactivity when calcination is carried out at high CO_2 vol.% and high temperature [7, 32]. The ratio of CaO Bragg peak (111) intensity to CaO (200) peak intensity is plotted in Fig. 6 as a function of calcination time. The horizontal dashed line indicates the relative intensity given by CaO (lime) reference patterns ($I_{111}/I_{200} = 0.389$) available from the Crystallography Open Database (COD) [37]. As can be seen, the relative intensity measured falls to this level once decarbonation is completed, which indicates that there is not a preferred orientation of crystallographic planes at the CaO surface. However, the results for the tests carried out at 890°C/70%CO_2 and 860°C/50%CO_2 (with a noticeable induction period and very slow decarbonation) illustrate that the ratio I_{111}/I_{200} is well over 0.389 when the CaO peaks start to appear. The diffractograms obtained from these tests are plotted in Fig. 3. Interestingly, the peaks located at the positions indicative of the CaO cubic lattice become already visible before $CaCO_3$ peaks intensity start to decline. This may be seen more clearly in Fig. 4, where the intensities of the Bragg $CaCO_3$ and CaO reflection peaks are plotted as a function of time for the calcination test at 860°C/50%CO_2. CaO reflection peaks appear 12 min after the calcination temperature is reached, but the decline of $CaCO_3$ (211) main peak intensity is not seen until 10-15 min later. For calcination at 890°C/70%CO_2 the intensity of the $CaCO_3$ peaks remains practically constant during the whole test whereas CaO peaks are clearly identifiable from $t \simeq 40$ min. These anomalies may be related to the formation of an intermediate CaO^* metastable structure (as early hypothesized by Hyatt et al. [9]) yielding reflections at the same angles that the parent $CaCO_3$ rhombohedral structure. Some works based on ex-situ XRD conventional analysis of calcined single $CaCO_3$ crystals under vacuum suggested that the metastable CaO^* form has the same structure of the cubic CaO stable lattice [18, 24, 38, 39]. However, the crystallographic relationships of the transformation are difficult to be drawn from either in-situ or ex-situ conventional XRD analysis [1]. Recent observations from transmission electron microscopy coupled with selected area electron diffraction (TEM-SAED) and 2D-XRD analyses on the decomposition of calcite single crystals [1] have confirmed that the reaction involves a crystallographic structural transformation as in the general class of topotactic transformations. Accordingly, decarbonation was seen to be initiated by the development of a mesoporous structure consisting of rod-shaped CaO^* nanocrystals on each rhombohedral cleavage face of the calcite pseudomorph. Subsequently, metastable CaO^* nanocrystals underwent oriented aggregation driven by surface attractive forces and became afterwards sintered. As the mesopores between the rod-shaped CaO^* nanocrystals were closed, CO_2 was desorbed to complete the transformation by the nucleation of stable CaO cubic crystals [1]. The kinetics of the transformation was observed to be determined by chemical decomposition since the desorption and structural transformation process proceeded extremely fast in the calcination tests, which were carried out under vacuum. Unfortunately, application of TEM-SAED to elucidate the details of the topotactic transformation is not feasible under high CO_2 partial pressure (technical progress in this direction would be a challenging task to pursue in future works).

IV. TG ANALYSIS

Figure 7 shows the thermograms obtained from the TGA calcination tests. As seen in the inset, the time evolution of $CaCO_3$ conversion α derived from these tests ($\alpha = (100/44)|\Delta wt|/wt_0$ where wt_0 is the initial $CaCO_3$ weight and Δwt is the weight loss) can be well fitted by a sigmoidal equation

$$\alpha = \frac{1}{1+\exp(-\beta(t-t_0))} \Leftrightarrow \frac{d\alpha}{dt} = f(\alpha)\beta(T,P) \tag{5}$$

with $f(\alpha) = \alpha(1-\alpha)$ according to a Prout-Tompkins mechanistic rate-equation and in agreement with Eq. 4 derived from the in-situ XRD analysis. A good fit is also obtained using the Avrami-Erofeev expression ($f(\alpha) = n(1-\alpha)\left[-\ln(1-\alpha)\right]^{1-1/n}$), which is extensively employed in kinetic studies [40, 41] and, as the Prout-Tompkins expression, also captures the existence of an induction period after which the reaction is started in structural defects. However, our main goal in the present work is not to analyze in detail the mechanistic-rate function $f(\alpha)$ that better fits to the data but the dependence of the decarbonation rate constant (β in Eq. 5) on temperature and CO_2 partial pressure. For this purpose, conversion time evolution data have been fitted to the simpler sigmoidal equation.

Figure 7 shows, also in qualitative agreement with the results derived from the in-situ XRD analysis, that decarbonation at close to equilibrium conditions (high CO_2 pressures and high temperatures) is slowed down as the temperature is increased. For a given value of conversion, the decarbonation rate $r \propto \beta$ is a decreasing function of temperature if P/P_{eq} is kept at a constant value.

V. REACTION KINETICS

According to the TGA and in-situ XRD analysis results presented, the conversion rate $(d\alpha/dt)$ can be expressed as the product of the functions $f(\alpha) \simeq \alpha(1-\alpha)$ and $\beta(T,P)$, the former one conforming to a Prout-Tompkins mechanistic model at the conditions of our experiments. We now focus on the formulation of a theoretical model for the dependence of the reaction rate on temperature T and CO_2 partial pressure, which can be retrieved experimentally from the separate function $\beta(T,P)$.

Let us assume the ideal situation of an infinite plane surface of a $CaCO_3$ solid undergoing decarbonation at uniform gas pressure and temperature. The kinetics of unimolecular surface reactions at these ideal conditions is often described by a mechanistic model consisting of chemical decomposition and desorption. Following this general concept, surface chemical decomposition gives rise to CaO and adsorbed CO_2, which is then desorbed from the surface:

1. **Chemical decomposition**

$$\mathrm{CaCO_3} + \underset{1-\phi}{L} \underset{k_2}{\overset{k_1}{\rightleftharpoons}} \mathrm{CaO} + \underset{\phi}{L(\mathrm{CO_2})}$$

Rate: $r_1 = k_1(1-\phi) - k_2\phi$

2. **Desorption**

$$\underset{\phi}{L(\mathrm{CO_2})} \underset{k_a}{\overset{k_d}{\rightleftharpoons}} \underset{1-\phi}{L} + \underset{P}{\mathrm{CO_2}(g)}$$

Rate: $r_d = k_d\phi - k_a(1-\phi)P$

Here L represents an active site and $L(CO_2)$ denotes an active site filled with a molecule of CO_2 that remains adsorbed after decomposition, ϕ is the fraction of active sites covering the surface which are occupied by CO_2, $(1-\phi)$ is the fraction of active sites empty, and k_i are the reaction rate constants. The activities of the solids are equal to 1. Thus, the reaction rate would be determined by the fraction of active sites filled ϕ (either by chemical decomposition or adsorption), the gaseous CO_2 partial pressure P and the reaction rate constants.

According to the microscopic reversibility general principle, the state of equilibrium is reached when the average rate of any process in each elementary step is equal to the average rate of its reverse process, which translated to decarbonation/cabonation and desorption/adsorption means that $r_1 = r_d = 0$ at equilibrium ($\phi = \phi_{eq}, P = P_{eq}$):

$$\begin{aligned} k_1(1-\phi_{eq}) &= k_2\phi_{eq} \qquad (6) \\ k_a(1-\phi_{eq})P_{eq} &= k_d\phi_{eq} \qquad (7) \end{aligned}$$

Thus,

$$P_{eq}(\mathrm{atm}) = \frac{k_1 k_d}{k_2 k_a} = K_1 K_d \qquad (8)$$

where $K_1 = k_1/k_2$ and $K_d = k_d/k_a$ are the decomposition and desorption thermodynamic equilibrium constants, respectively, that can be expressed by means of the van't Hoff equation:

$$\begin{aligned} K_1 &= A_1 \exp(-\Delta_1 H^0/RT) \qquad (9) \\ K_d &= A_d \exp(-\Delta_d H^0/RT) \qquad (10) \end{aligned}$$

where $\Delta_1 H^0$ and $\Delta_d H^0$ are the standard enthalpy change for decomposition and desorption, respectively. The pre-exponential factors are given by $A_1 = \exp(\Delta_1 S^0/R)$ and

$A_d = \exp(\Delta_d S^0/R)$, where $\Delta_1 S^0$ and $\Delta_d S^0$ are the standard entropy changes of decomposition and desorption, respectively.

Using the empirical equation for P_{eq} (Eq. 3) in Eq. 8, the standard enthalpy and entropy changes for the overall decarbonation reaction would be $\Delta_r H^0 = \Delta_1 H^0 + \Delta_d H^0 = 170.2$ kJ/mol and $\Delta_r S^0 = \Delta_1 S^0 + \Delta_d S^0 = 145.7$ J/mol-K, which are close to the values of the standard enthalpy and entropy of the overall reaction derived from thermodynamic analysis ($\Delta_r H^0 \simeq 177.8$ kJ/mol and $\Delta_r S^0 \simeq 160.4$ J/mol-K) [2, 11, 42]. Desorption is normally an endothermic process ($\Delta_d H > 0$ with little variation on temperature) as it involves overcoming a physical bond between the solid surface and the gas usually arising from attractive van der Waals forces. Since these forces are much less strong than chemical bonding, desorption enthalpy changes are low (of the order of 20 kJ/mol) as compared with the enthalpy change associated to chemical decomposition [43]. Taking the enthalpy change of CO_2 desorption as $\Delta_d H^0 = 20$ kJ/mol, the value of the decomposition enthalpy change would be $\Delta_1 H^0 \simeq 150$ kJ/mol.

The pseudo-steady state hypothesis states that there is not a net accumulation of reactive intermediates [44], which implies in our case that the increase rate of the fraction of active sites filled with CO_2 by decomposition must equal the rate of desorption ($r_1 = r_d$):

$$\frac{d\phi}{dt} = 0 \Rightarrow \phi = \frac{k_1 + k_a P}{k_1 + k_2 + k_d + k_a P} \tag{11}$$

Let us analyze the dependence of the reaction rate on temperature and CO_2 partial pressure. In most gas-solid heterogenous reactions that are not diffusion-limited, desorption is usually a fast process as compatred to chemical decomposition (k_1, $k_2 << k_d$, $k_a P$). Thus, from Eq. 11 it is

$$\phi \approx \frac{k_a P}{k_d + k_a P} = \frac{K_a P}{1 + K_a P} \tag{12}$$

where $K_a = 1/K_d$. Note that Eq. 12 conforms to the Langmuir isotherm equation for adsorption. Using Eq. 8 the overall reaction rate can be written as

$$r \approx r_1 = k_1(1-\phi) - k_2\phi = k_1\left(1 - \frac{P}{P_{eq}}\right)(1-\phi) \approx k_1\left(1 - \frac{P}{P_{eq}}\right)\frac{1}{1 + K_1 P/P_{eq}} \tag{13}$$

The rate constant k_1 follows an Arrhenius law

$$k_1 = a_1 \exp(-E_1/RT) \tag{14}$$

where $E_1 > 0$ is the activation energy for decomposition and a_1 is a pre-exponential factor, which yields

$$r \approx a_1 \exp(-E_1/RT)\left(1 - \frac{P}{P_{eq}}\right)\frac{1}{1 + A_1 \exp(-\Delta_1 H^0/RT)P/P_{eq}} \tag{15}$$

At very low CO_2 partial pressures or low calcination temperatures it is $K_a P = K_1 P/P_{eq} << 1$ and the fraction of active sites filled with adsorbed CO_2 molecules is small ($\phi << 1$ in Eq. 12). In this limit the reaction rate predicted is

$$r \approx a_1 \exp(-E_1/RT)\left(1 - \frac{P}{P_{eq}}\right) \tag{16}$$

which conforms to Eq. 2 commonly employed as a good fit to experimental data on the rate of decarbonation (usually performed at $P << P_{eq}$) and yielding activation energies around the overall reaction enthalpy change (although in a widely scattered range between 100 and 230 kJ/mol [22]). Thus, the reaction rate increases with temperature following an Arrhenius law controlled by the activation energy of chemical decomposition E_1.

In the opposed limit ($K_aP = K_1P/P_{eq} >> 1 \leftrightarrow (1-\phi) \approx 1/(K_aP)$), which may be met only at very high temperatures ($K_1 >> 1$) and not small CO_2 partial pressures, the predicted reaction rate would be

$$r \approx a_2 \exp(-E_2/RT)\left(\frac{P_{eq}}{P} - 1\right) \tag{17}$$

where $E_2 = E_1 - \Delta_1 H^0$ is the activation energy for the carbonation chemical reaction.

Since the activation energy usually measured for calcination at $P/P_{eq} << 1$ is close to the overall reaction enthalpy change derived from thermodynamic analysis ($E_1 \simeq \Delta_r H^0$), it might be thought that the activation energy for carbonation E_2 is close to zero as postulated in previous works [45] where the desorption/adsorption step is obviated. However, recent experimental measurements [42] on the carbonation kinetics yield a non-negligible carbonation activation energy $E_2 = 24 \pm 6$ kJ/mol. This value is entirely consistent with a decomposition enthalpy change $\Delta_1 H^0 = \Delta_r H^0 - \Delta_d H^0 \simeq 150$ kJ/mol where $\Delta_d H^0 \simeq 20$ kJ/mol as assumed above. Thus, Eq. 17 would predict also an increase of the reaction rate with temperature at high CO_2 pressures but at a lower rate ($E_2 \simeq 20$ kJ/mol) as compared with the predicted rate from Eq. 16.

Let us now explore the possibility that the slowest rate-limiting step in decarbonation is CO_2 desorption (k_1, $k_2 >> k_d, k_aP$). In that case the overall reaction rate would be given by the rate of desorption

$$r \approx k_d\phi - k_a(1-\phi)P \tag{18}$$

with the fraction of active sites filled with CO_2 determined by the chemical reaction rate constants (Eq. 11):

$$\phi \approx \frac{k_1}{k_1 + k_2} = \frac{1}{1 + 1/K_1} \tag{19}$$

Thus,

$$r \approx k_d \left(1 - \frac{P}{P_{eq}}\right) \phi \approx a_d \exp(-E_d/RT) \left(1 - \frac{P}{P_{eq}}\right) \frac{1}{1 + \exp(\Delta_1 H^0/RT)/A_1} \tag{20}$$

where E_d is the activation energy for desorption and a_d is a pre-exponential factor. According to Eq. 19, in the limit $K_1 = K_a P_{eq} >> 1$ the fraction of active sites occupied by CO_2 would be large ($\phi \simeq 1$) and the reaction rate would depend mainly on T through k_d increasing with temperature following an Arrhenius law determined by the activation energy of desorption E_d:

$$r \approx a_d \exp(-E_d/RT) \left(1 - \frac{P}{P_{eq}}\right) \tag{21}$$

Since the activation energy of adsorption E_a is in general not appreciable [43], it would be $E_d = E_a + \Delta_d H^0 \simeq 20$ kJ/mol.

In the limit $K_1 = K_a P_{eq} << 1$ it is $\phi << 1$ (Eq. 19), and the reaction rate would be

$$r \approx a_d A_1 \exp(-(E_d + \Delta_1 H^0)/RT) \left(1 - \frac{P}{P_{eq}}\right) \tag{22}$$

where $E_d + \Delta_1 H^0 \simeq \Delta_r H^0 \simeq 170$ kJ/mol.

A. The role of structural transformation

None of the above mechanisms would predict a decrease of the reaction rate with temperature at constant P/P_{eq} as inferred from our calcination tests nearby equilibrium. However, the experimentally observed transformation from the metastable CaO form (CaO*) to the stable CaO form as CO_2 is desorbed has not been yet considered. As detailed in the study reported in [18] on calcite decarbonation under vacuum, desorbed CO_2 molecules must escape out from the reaction surface by diffusion through the metastable CaO* porous network. An estimation of the fraction of desorbed CO_2 molecules that passes across a porous barrier is given by [18]

$$\Lambda = \frac{\Gamma}{\Gamma + \epsilon} \tag{23}$$

where Γ is the probability that a CO_2 molecule emerges out of the barrier by diffusion without coming back and ϵ is the probability that a returned CO_2 molecule reacts back. According to the principle of microscopic reversibility, the partial pressure of CO_2 inside the CaO* pores (P_{int}) would be close to the equilibrium pressure $P_{int} \sim P_{eq}$ regardless of the CO_2 partial pressure in the surrounding environment P. If P is very small ($P/P_{eq} << 1$), it would be $P_{int} >> P$ and the value of Γ may be simply estimated from a Knudsen diffusion process as the ratio of the pore size to the barrier thickness, which is typically much larger than ϵ [18]. Therefore, desorption can be dismissed for calcination under vacuum as recently confirmed by in-situ observations showing that there is no significant resistance against the outwards diffusion of CO_2, which was seen to escape out from the porous metastable CaO* very quickly [1]. Thus, chemical decomposition determines the reaction kinetics for calcination under very small CO_2 partial pressures ($P/P_{eq} << 1$). The scenario may change however for calcination at high CO_2 partial pressures. Under this condition, the leakage of CO_2 molecules through the metastable structure would be hampered according to Fick's law since the gradient between the CO_2 pressure inside the porous network and outside is small. CO_2 desorption and the concomitant transformation of the metastable CaO* to CaO should be considered as a further necessary step of the reaction for decarbonation to be completely achieved:

1. **Chemical decomposition**

$$\mathrm{CaCO_3} + \underset{1-\phi}{L} \underset{k_2}{\overset{k_1}{\rightleftharpoons}} \underset{a^*}{\mathrm{CaO}^*} + \underset{\phi}{L(\mathrm{CO_2})}$$

2. **Desorption and structural transformation**

$$\underset{a^*}{\mathrm{CaO}^*} + \underset{\phi}{L(\mathrm{CO_2})} \underset{k_a}{\overset{k_d}{\rightleftharpoons}} \mathrm{CaO} + \underset{1-\phi}{L} + \underset{P}{\mathrm{CO_2}(g)}$$

where a^* stands for the activity of the metastable CaO* form. In general, whenever the direct solid product of a decomposition reaction is a metastable crystal modification or an amorphous form, the activity of this solid cannot be taken as unity but [46]

$$a^* = \exp(\Delta G_*/RT) \tag{24}$$

where $\Delta G_* = \Delta H_* - T\Delta S_*$ is the positive free energy of formation of the metastable form from the stable form. The enthalpy change ΔH_* would be the energy relieved when the metastable CaO* structure collapses after desorption into the stable CaO structure, which has been estimated elsewhere as ΔH_* ~50 kJ/mol from calcination tests under vacuum [18, 46, 47]. Formally, the predicted rates are the same as above but replacing the rate constants k_2 and k_d by k_2a^* and k_da^*, respectively. The overall reaction rate at high values of P/P_{eq} would be then

$$r \approx a_d A_* \exp(-(E_d - \Delta H_*)/RT) \left(1 - \frac{P}{P_{eq}}\right) \phi \tag{25}$$

$$\phi \approx \frac{1}{1 + \exp((\Delta_1 G^0 + \Delta G_*)/RT)} \tag{26}$$

where $A_* = \exp(-\Delta S_*/R)$ and $\Delta_1 G^0 = \Delta_1 H^0 - T\Delta_1 S^0$. In the limit $\phi \simeq 1$, which would be the case at high temperatures, the reaction rate would be given by

$$r \approx a_d A_* \exp(-(E_d - \Delta H_*)/RT) \left(1 - \frac{P}{P_{eq}}\right) \tag{27}$$

Since expectedly it is $E_d - \Delta H_* < 0$, the reaction rate would be decreased with temperature at constant P/P_{eq} as observed in our tests. As the temperature is lowered down the fraction ϕ decreases and in the limit $\phi << 1$ $(\exp((\Delta_1 G^0 + \Delta G_*)/RT) >> 1)$ the reaction rate predicted would be

$$r \approx a_d A_1 \exp(-(E_d + \Delta_1 H^0)/RT) \left(1 - \frac{P}{P_{eq}}\right) \tag{28}$$

which decreases with temperature ($E_d + \Delta_1 H^0 \simeq 170$ kJ/mol). According to this mechanism we would observe an increase of the reaction rate with $1/T$ at high temperatures with a progressively decreasing rate as $1/T$ is increased and ϕ decreases. At a certain critical temperature the reaction rate reaches a maximum and turns to decrease with $1/T$.

Let us compare the α-independent reaction rate factor $\beta(T, P) \sim r$ measured from our XRD and TGA tests with the reaction rates theoretically predicted. Measured values of $\beta/(1 - P/P_{eq})$ are plotted in Fig. 8 as a function of $1/T$. The trends plotted ($r \propto \exp(-E/RT)$) are the theoretical predictions from Eq. 27 (using $E = -30$ kJ/mol and -200 kJ/mol), Eqs. 17 and 21 ($E = 20$ kJ/mol), and Eqs. 16, 22 and 28 ($E = 170$ kJ/mol). In spite of the data scatter, Fig. 8 shows that for high temperatures ($T \gtrsim 830$°C) the reaction rate clearly increases with $1/T$ in agreement with Eq. 27 ($\phi \simeq 1$). A good fit is obtained for $E = -200$ kJ/mol suggesting a value for the enthalpy change of structural transformation $\Delta H_* \sim 220$ kJ/mol. Interestingly, it is seen in Fig. 8 that the increase of the reaction rate with $1/T$ slows down at lower temperatures which could be explained by a decrease of ϕ with $1/T$ (Eq. 26). In our tests, the ratio P/P_{eq} varies in a window between 0.6 and 0.85. Further experiments in narrower windows of P/P_{eq} might help reducing the experimental data scatter as well as identifying more clearly the role of the diverse mechanisms on the reaction rate. The difficulty of these measurements resides in the control of phenomena such as temperature gradients in the solid or internal mass/heat transfer effects that are specially relevant for calcination under high CO_2 partial pressures [16, 48]. For example, thermal diffusion may affect the reaction kinetics due to temperature differences of a few °C between the interior of the solid and its external surface caused by the endothermicity of the reaction [48]. This can be relevant if the reaction is hindered by outwards CO_2 diffusion when the CO_2 partial pressure in the surrounding environment is close to the equilibrium pressure. To overcome this burden and simplify the kinetic analysis most studies reported in the literature are carried out in the limit $P/P_{eq} << 1$. Yet the study of calcination at high CO_2 pressure and high temperatures has gained a remarkable interest from recently emerged applications such as the Ca-looping for post-combustion CO_2 capture. Our results show that, at these conditions, the decarbonation rate is decreased with temperature (at least in a certain range of high temperatures/high CO_2 partial pressures). Additional research on the kinetics of calcination nearby equilibrium should be pursued in future studies to further explore this result.

VI. CaO CHARACTERIZATION

In this section we investigate the structural properties and chemical reactivity of CaO resulting from limestone calcination as influenced by the calcination temperature and CO_2 partial pressure at the conditions of our tests close to equilibrium.

A. CaO crystallite size

In-situ XRD tests allow us obtaining the time evolution of the CaO coherently diffracting domain size (usually known as crystallite size L_c) by means of the Scherrer equation

$$L_c = \frac{\kappa\,\lambda}{\beta\cos\theta} \tag{29}$$

where $2\theta \simeq 37.1^\circ$ is the Bragg angle of the most intense CaO reflection peak (200), κ is a dimensionless shape factor ($\kappa = 0.89$ for the CaO cubic structure), and β (in radians) is the line broadening at half the maximum intensity (full width at half maximum FWHM). Line broadening has been corrected by the instrumental width $\beta_0 \simeq 0.132$, which was obtained from the XRD pattern of certified LaB_6. Thus, it is $\beta = [\beta_M^d - \beta_0^d]^{1/2}$, where β_M is the experimentally measured FWHM and $d = 2$ since the peak shape conforms approximately to a Gaussian distribution.

Figure 9 shows the time evolution of the CaO crystallite size L_c during calcination. We see that L_c is mainly determined by its initial value and changes only slightly as calcination progresses. The most determining parameter is the CO_2 partial pressure, whose increase leads in general to an increase of L_c. For values of the CO_2 vol.% below 30%, L_c shows a moderate increase with the calcination time and increases as the calcination temperature is risen. On the other hand, a diverse trend is observed for the samples calcined at higher CO_2

vol.%. In this range of high CO_2 partial pressures, L_c reaches a relatively high value as soon as CaO peaks are detected and decreases slightly with the calcination time. Moreover, for a given value of high CO_2 vol.%, L_c is increased as the calcination temperature is diminished. For example, the average value of L_c is 34 nm for the sample calcined at 900°C under 70%CO_2 whereas it is $\langle L_c \rangle \simeq 41$ nm when the calcination temperature is 890°C and the reaction kinetics is considerably slowed down (see Figs. 5 and 7). This observation supports a sintering mechanism near equilibrium according to which the nascent CaO crystallites are initially formed by aggregation of metastable CaO_* nanocrystals and sintering afterwards. Under high CO_2 vol.%, the aggregation step would be enhanced by a slower reaction kinetics at smaller temperatures since CO_2 desorption and structural transformation are hindered. Moreover, a high fraction of active sites filled with CO_2 molecules adsorbed on the surface of the CaO^* nanocrystals during this very slow process ($\phi \simeq 1$) would give rise to a significant increase of their surface energy [49] and therefore would enhance the attractive force between them. This would yield an enlargement of the CaO coherent crystal length when the unstable structure collapses into the stable CaO form and CO_2 molecules are desorbed. On the other hand, the dominant mechanism at low CO_2 partial pressures for CaO crystal growth would be sintering of the nanocrystals by lattice diffusion which is promoted by an increase of temperature. Accordingly, we see larger crystallites as the temperature is increased in the calcination tests at low CO_2 vol.%.

B. CaO sintering

Representative SEM images of samples calcined in the XRD chamber at diverse conditions of temperature and CO_2 vol.% are displayed in Fig. 10. As may be seen, an increase of temperature and CO_2 vol.% yields a noticeable decrease of porosity and an increase of grain size as well documented from previous studies (albeit in previous works calcination conditions are generally far from equilibrium: $P/P_{eq} << 1$) [21, 50, 51]. Average values of the grain size d derived from a statistical analysis of SEM images are plotted in Fig. 11a showing a clear correlation between d and the CO_2 partial pressure which fits approximately to a linear increase law. In contrast with the decrease observed for the crystallite size L_c with temperature at high CO_2 partial pressure, we see that d is an increasing function of temperature independently of the CO_2 vol.% (see the inset of Fig. 11a). After formation of the stable CaO crystallites, the sintering process should be driven by the subsequent agglomeration of these crystallites into polycrystalline CaO grains and the parallel closure of small pores. Further agglomeration of the polycrystalline CaO grains as calcination progresses would be favored by temperature enhanced lattice diffusion. Figure 11b demonstrates a clear quantitative correlation between the ratio of CaO grain size to crystallite size with the CO_2 vol.% (CO_2 vol.%$\approx P$ (kPa) in our tests at atmospheric pressure), which is rather well adjusted by the linear law

$$\frac{d}{L_c} \simeq 1 + 0.4P \tag{30}$$

Extrapolating this law to $P = 0$ it is predicted $d_0 \simeq L_{c0}$, which suggests that, in the absence of CO_2, sintering is precluded and the CaO structure resulting from calcination would consist of mono-crystalline CaO nanograins with very high surface area as observed in experiments where calcination is carried out under vacuum (at temperatures as high as 1050°C) [47]. As was shown in [47], XRD patterns of CaO resulting from calcination under vacuum exhibit very weak diffraction peaks indicative of the production of CaO crystallites of size ~ 10 nm regardless of the calcination temperature. This supports the argument that aggregation of the CaO* nanocrystals, which is enhanced by promoted surface energy due to adsorbed

CO_2, plays a main role on the enhanced sintering of CaO calcined under high CO_2 partial pressure.

The agglomeration and growth of CaO polycrystalline grains must be accompanied by the closure of small pores and therefore by a reduction of the surface area. Pore size distributions obtained for our calcined samples from N_2 physisorption (77 K) analysis are shown in Fig. 12. As can be seen, the pore area is drastically reduced as the CO_2 vol.% is increased above 30%, which causes that a major fraction of the pores grow up to a size larger than the upper limit detectable by the N_2 physisorption technique ($\sim$200 nm). Consequently, values of the BET surface area obtained S_{BET} for the samples calcined under CO_2 vol.% above 50% are below the accuracy of the technique, which is about 1 m^2/g. Alternatively, a rough estimation of the surface area may be inferred by approximating the CaO grains of size d derived from the SEM analysis (Fig. 11) to smooth spheres [50], which gives $S_d \sim 6/(\rho_{CaO} d)$ where $\rho_{CaO} = 3.37$ g/cm^3 is CaO solid density. Figure 13a shows S_{BET} and S_d as a function of grain size. Taking into account the experimental indeterminacy, there is an acceptable agreement between both data sets. The surface area of the samples calcined under CO_2 vol.%>50% is estimated to be close to the residual surface area for limestone derived CaO ($S_r \sim 1$ m^2/g) [52]. Additional physisorption tests on the calcined samples were carried out in our work using Kr (77 K) instead of N_2, which generally gives better results for samples with low surface area. Values measured of S_{BET} using Kr are plotted in Fig. 14 showing that CaO attains a residual surface area as expected of about 1 m^2/g at severe calcination conditions.

Most of the data published in the literature on the variation of CaO surface area ΔS with calcination time t_s [21] conforms reasonably well to the German-Munir equation [53],

$$\frac{\Delta S}{S_0} = (K_s t_s)^{1/\gamma_s} \tag{31}$$

where S_0 is the initial surface area, the sintering constant K_s follows an Arrhenius law type dependence on temperature and the exponent γ_s is related to the main mechanism responsible for sintering. The German-Munir model assumes that CaO grains with initially spherical shape sinter by formation of a neck at contact points, which grows in diameter as matter is transported to the neck region by several possible mechanisms. For calcination in an inert atmosphere, the transport mechanism depends generally on the calcination temperature as compared to the melting temperature T_m of the material [54]. In the usual range of calcination temperatures for CaO ($T_m = 2886$ K) between 700°C and 1000°C, it is $0.33T_m \lesssim T \lesssim 0.44T_m$ (in K), which would imply that sintering should occur by surface diffusion of chemical constituents [54]. Sintering by lattice diffusion is initiated in most materials at the so-called Tamman temperature T_t (around half the melting temperature in K), which is $T_t \simeq 1170$°C for CaO [54]. Diffusion of chemical species across the crystalline lattice would become noticeable only above this temperature, which is well over the range of common limestone calcination temperatures. Yet, sintering rates of limestone derived CaO for calcination under pure N_2 (in the temperature range between 700°C and 1100 °C) agrees with the prediction by Eq. 31 for $\gamma_s \simeq 2.7$ suggesting that transport of matter does occur by lattice diffusion mechanism [50], which is attributed to the acceleration of solid-state-diffusion by impurities and lattice defects. Results from calcination of ultrapure $CaCO_3$ large monocrystals yielded slower sintering rates more consistent with surface (instead or lattice) diffusion [50] as expected. On the other hand, CaO sintering is greatly enhanced by the presence of CO_2 in the calcination atmosphere, which is a well documented observation [21, 51, 55, 56] albeit most experiments are carried out in the regime $P/P_{eq} << 1$. The sintering constant K_s and exponent γ_s that fit most of the experimental data are given by

$$K_s = 1.08 \times 10^8 \, P^{0.558} \exp(-30000/T) \tag{32}$$

$$\gamma_s = 44.1(0.8 \ln P - 1) \exp(-4140/T) \tag{33}$$

(missprints in the equations presented in the original work [51] are noted in a later review [21]). Here P is in Pa, the temperature T is in K and K_s in min^{-1}. Experimental data are fitted by using values of γ_s well over 10, which indicates a strong influence of extraordinary sintering mechanism(s) induced by the presence of CO_2 not well understood yet. Likewise, water vapor leads to a marked catalyzing effect of sintering [51].

The German-Munir model [53] is based on the assumption that the nascent CaO forms an open array of grains that coalesce via neck formation and growth at contact points. Under the restriction $|\Delta S/S_0| < 0.5$, the curvature gradient in the neck region yields a relative decrease of the surface area given by Eq. 31. Equations 31-33 yield unreasonable values for $|\Delta S/S_0|$ in the CO_2 partial pressure and temperature conditions of our tests. Moreover, Eq. 31 cannot account for the approach to a residual value S_r for long sintering times as observed experimentally. This is taken into account by the empirical general power law expression (GPLE) originally derived to describe the sintering and deactivation of supported metal catalysts [57]

$$-\frac{d}{dt}\frac{S}{S_0} = k_s \left(\frac{S}{S_0} - \frac{S_r}{S_0}\right)^m \Rightarrow S \approx S_0 \frac{1 + k_s t_s S_r/S_0}{1 + k_s t_s} \tag{34}$$

where it has been applied m =2 valid for sintering processes governed by lattice diffusion [57], k_s is a sintering constant and we have used $S_r/S_0 << 1$. Equation 34 has been employed to fit experimental data on CaO sintering [21, 58] with k_s following an Arrhenius type law at low CO_2 partial pressures [21]. Equation 34 has served to predict the loss of CaO carbonation activity in the surface reaction controlled regime as it is subjected to a long series of carbonation/calcination cycles by assuming that the carbonation reactivity scales proportionally to the surface area [59, 60] (this point will be addressed below in further detail). The surface area of the nanostructured CaO just before sintering starts ($S = S_0$) has been estimated elsewhere as $S_0 = 104$ m^2/g from measurements on samples taken immediately after calcination in air at 700°C [50], which agrees with estimations on the surface area of the metastable CaO_* nanocrystals [18, 61] (in agreement with the prediction $d_0 \simeq L_{c0}$ from Eq. 31). Using $S_0 = 104$ m^2/g and $S_r = 1$ m^2/g in Eq. 34 we find a good fit to our experimental data on S (Fig. 13b) for a sintering constant k_s ten times the sintering constant K_s reported for relatively low CO_2 partial pressures (Eq. 32). A possible explanation for the catalyzing effect of CO_2 on sintering (particularly relevant at CO_2 pressures near the equilibrium pressure) is that CO_2 molecules physically adsorbed on the surface of the grains leads to a great enhancement of surface energy, which would promote the agglomeration of the grains.

Further simplification of Eq. 34 allowed by $S_r/S_0 \sim 0.01 << 1$ leads to the simple equation $S/S_0 \approx 1/(1 + k_s t_s)$ for short sintering times. Since $S \propto d$, we arrive also at $d/d_0 \simeq (1 + k_s t_s)$ with $k_s \simeq 10^9 \times P^{0.5} \exp(-E_s/RT)$ min^{-1}, an activation energy for sintering $E_s \simeq 250$ kJ/mol, and $d_0 \simeq 15$ nm for the CaO grain size in the absence of CO_2 in the calcination atmosphere (estimated using $S_0 \sim 100$ m^2/g for uniform spheres with no connecting necks) and equal to CaO crystallite size. From a practical perspective, sintering at high CO_2 partial pressure might be mitigated by placing in the lattice thermally stable inert nanocrystals that would minimize aggregation of the CaO^* nanocrystals and CaO grains. This could be for example the role played by MgO nanocrystallites in calcined dolomite ($CaMg(CaCO_3)_2$) [30] and mayenite nanocrystallites in synthetic CaO/mayenite composites [62], which help mitigating CaO sintering as observed experimentally.

C. CaO reactivity

Let us finally analyze the effect of calcination conditions on the reverse carbonation reaction, which would take place if the temperature and CO_2 pressure are changed to shift the reaction towards carbonation. Carbonation of CaO is initiated by a reaction-controlled phase on the surface of the CaO grains until a thin layer of $CaCO_3$ (between 30 and 50 nm thick [35, 63, 64]) is developed, which leads to a much slower phase driven by the counter-current diffusion of inward CO_3^{2-} anion groups and outward O^{2-} anions through the carbonated layer [35, 63, 65]. From our in-situ XRD analysis we may infer that the CaO structure that results after full calcination does not have a preferential crystallographic direction oriented normal to the exposed surface, which might have an influence on the CaO carbonation reactivity in the reaction controlled phase as was suggested in previous studies [7, 31–33]. We now investigate whether the poor carbonation reactivity of CaO resulting from calcination under high CO_2 vol.% reported in previous works [7] can be solely explained by the decrease of CaO surface area as a consequence of enhanced sintering.

Figure 15a shows data on CaO conversion in the reaction controlled phase X_r measured in our TGA tests by carbonation in-situ at 650°C/15%CO_2 (typical conditions of post-combustion CO_2 capture [2]) as a function of grain size d (derived from the SEM analysis). The inset of Fig. 15a illustrates the time evolution of sample weight during carbonation. As may be seen, the end of the reaction controlled fast phase and beginning of the diffusion controlled slow phase is clearly distinguishable. Figure 15a demonstrates that X_r is well correlated to sintering and is approximately proportional to the inverse of CaO grain size d.

Thus, it may be inferred that X_r scales proportionally to the CaO surface area available for carbonation as assumed in previous modeling studies [66]. Interestingly, an extrapolation of the results to the grain size lower limit suggests that all CaO available would be converted in the reaction controlled phase if grain size were below a value of around 50 nm as would be the case of CaO derived from calcination at relatively low temperature and low CO_2 partial pressure or under vacuum.

By assuming that for large CaO grains the reaction surface of area S is flat and that the reaction controlled phase ends up when a thin layer of thickness h is formed on the surface, CaO conversion in this phase could be estimated using the simple equation

$$X_r = \left[\frac{M_{CaO}}{M_{CaCO3}} \rho_{\mathrm{CaCO3}} h \right] S \tag{35}$$

where M_{CaO}/M_{CaCO3} is the ratio of CaO/$CaCO_3$ molecular weights and $\rho_{CaCO3} = 2.7$ g/cm^3 is the $CaCO_3$ solid density. CaO conversion results predicted from Eq. 35, using the estimated values of surface area from grain size (S_d) and $h = 40$ nm, are plotted in Fig. 15b versus the X_r data experimentally measured. As may be seen, there is a good agreement between predicted and measured data. Equation 35 gives however unrealistic conversions above one for $S_d \gtrsim 17$ m^2/g (d $\lesssim$100 nm). In this case, the flat surface assumption leading to Eq. 35 is not justified and more sophisticated models have to be developed [35, 64, 67]. Moreover, the closure of small pores by $CaCO_3$ limits the carbonation reaction before diffusion becomes rate-limiting.

Our work shows that, in the conditions of our tests, and regardless of CO_2 partial pressure and temperature, there is not a preferential growth of the CaO surface along poorly reactive (200) planes as has been suggested from theoretical studies [32]. Thus, the very small carbonation reactivity of CaO derived from calcination under high temperature and CO_2

concentration may be explained just by the considerable reduction of surface area as a consequence of sintering. It can be noticed that CaO conversion in the reaction controlled phase for the samples calcined under the most severe conditions is close to 0.1 (Fig. 15), which is close to the residual conversion seen when limestone derived CaO is subjected to a long series of carbonation/calcination cycles [59, 66]. Accordingly, we see that the surface area of these samples calcined under hash conditions is reduced to a value near the residual value of $\sim$1 m^2/g (Fig. 13). It remains to be explained the drastic drop of CaO conversion experienced by samples precalcined in air and subsequently subjected to carbonation/calcination cycles in which calcination is carried out under high CO_2 vol.% and high temperature [7]. CaO conversion in these tests dropped in just about 10 cycles to a value of about half the value of conversion corresponding to the residual CaO surface area. The type of precalcination atmosphere in those tests was crucial for CaO conversion in the reaction controlled phase to drop to such a small value. If precalcination was carried out also under high CO_2 vol.%, CaO conversion reached a residual value close to 0.1 as corresponds to CaO residual surface area. The possibility that CaO resulting from regeneration in multiple carbonation/calcination tests grow preferentially along planes with low reactivity has yet to be explored. At this moment, technical difficulties related to low heating rates in the XRD temperature chamber precludes us from carrying out an in-situ XRD study at realistic Ca-looping conditions, which necessarily imply very fast changes of temperature between the carbonation and calcination stages.

VII. CONCLUSIONS

In this work we have analyzed the influence of CO_2 partial pressure on limestone decomposition nearby equilibrium in order to explore the fundamental mechanisms governing the reaction at these conditions. Results from in-situ XRD analysis and TGA tests show that the conversion rate $d\alpha/dt$ can be expressed as the product of a conversion independent reaction rate $\beta(T, P)$ and a function of conversion $f(\alpha) = \alpha(1 - \alpha)$, which conforms to a Prout-Tompkins mechanistic rate-equation. The reaction rate is decreased by an increase of temperature if the ratio of CO_2 partial pressure to equilibrium pressure is kept constant and high ($P/P_{eq} \gtrsim 0.6$). This observation may be explained by a reaction mechanism in which hindered CO_2 desorption and (exothermic) CaO*/CaO structural transformation are a further necessary step for decarbonation to be completed. Arguably, the reaction would be initiated after an induction period in certain active sites located at crystal defects where the outwards diffusion of desorbed CO_2 is favored, which agrees with observations reported elsewhere on the effect of limestone crystallinity on the reaction rate at high CO_2 partial pressure [8]. Once initiated, conversion is accelerated as it progresses, presumably helped by the exothermicity of the structural transformation, until it reaches a maximum rate and slows down when approaching its end.

In regards to CaO sintering during calcination, in-situ XRD analysis and SEM observations show that the great reduction of CaO surface area after calcination at high CO_2 partial pressure and high temperature is mainly caused by CaO grain agglomeration and not crystal growth. The size of CaO crystallites in the stable cubic form increase with the CO_2 partial pressure from $L_c \sim$20 nm at low pressures to $L_c\sim$40 nm at high pressure. Van der Waals attractive forces between the CaO* nanocrystals would be enhanced by adsorbed CO_2 molecules whose desorption is hindered at high CO_2 partial pressure, which promotes aggregation of these metastable nanocrystals and gives rise to stable CaO crystallites of larger size. An extrapolation of our results gives $d_0 \simeq L_{c0}$ for calcination in the absence of CO_2 ($P = 0$), which is in accordance with observations reported elsewhere on calcination under vacuum giving rise to a large surface area nanostructured CaO with very high carbonation reactivity. According to our observations the size of stable CaO crystallites do not change appreciably as the calcination time is increased, which supports the idea that their formation is mainly determined by agglomeration during the transformation of the metastable CaO* structure. On the other hand, the size of polycrystalline CaO grains d, which would result from agglomeration and sintering of the CaO crystallites during the calcination period, show a marked increase from $d \sim 50$ nm at low CO_2 partial pressure/low calcination temperature (close to the crystallite size) to $d = d_{max} \sim 1000$ nm at high CO_2 partial pressure/high calcination temperature, which leads to an estimated surface area close to a residual surface area of ~ 1 m^2/g as measured experimentally. Under the conditions of our experiments, our results are consistent with a sintering mechanism based on CaO grain growth by lattice diffusion and enhanced by the increase of surface energy due to CO_2 adsorption on the CaO grains. The evolution of grain size with the calcination time (t_s) may be adjusted for short sintering times by the simple empirical law: $d \sim d_0(1 + k_s t_s)$ with $k_s \simeq 10^9 \times P^{0.5} \exp(-E_s/RT)$ min^{-1} (P in Pa), $E_s \simeq 250$ kJ/mol (activation energy for sintering), and $d_0 \simeq 15$ nm.

The reactivity of CaO produced by calcination in our tests scales proportionally to the CaO surface area and therefore is severely hindered by the presence of CO_2 at high partial pressure. Our in-situ XRD analysis shows that the CaO surface does not grow preferentially along poorly reactive crystallographic planes as suggested in recent theoretical works even though further analysis must be carried out to check this observation in the case of CaO resulting from multiple carbonation/calcination cycles. Thus, CaO reactivity approaches a residual value, which is determined by the residual surface area. Aggregation of nanocrystals during the transformation would be hindered by the presence of thermally stable inert nanograins, which would prevent sintering and therefore the loss of CaO carbonation reactivity as seen for $CaO \cdot MgO$ derived from dolomite calcination and for synthetic CaO-based composites. Moreover, $CaCO_3$ decarbonation in these composites would be accelerated as observed experimentally [30] since crystal impurities promote diffusion of desorbed CO_2 and metastable CaO^* therefore enhancing the desorption/structural transformation step at CO_2 partial pressures close to equilibrium.

VIII. ACKNOWLEDGEMENTS

This work was supported by the Andalusian Regional Government Junta de Andalucia (contracts FQM-5735 and TEP-7858), Spanish Government Agency Ministerio de Economia y Competitividad and FEDER funds (contracts FIS2011-25161 and CTQ2011-27626). One of the authors (PESJ) is supported by the Juan de la Cierva program of the Spanish Ministerio de Economia y Competitividad. We gratefully acknowledge the Microscopy, Functional Characterization and X-ray services of the Innovation, Technology and Research Center of the University of Seville (CITIUS). The help from Drs. Santiago Medina, Javier Quispe and Francisco M. Varela (CITIUS) is specially recognized. Collaboration from Professor Joaquin Bastida, who kindly provided us with the LaB_6 certified sample, is warmly appreciated.

IX. REFERENCES

---

[1] C. Rrodriguez-Navarro, E. Ruiz-Agudo, A. Luque, A. B. Navarro, and M. Ortega-Huertas, “Thermal decomposition of calcite: Mechanisms of formation and textural evolution of cao nanocrystals,” *American Mineralogist*, vol. 94, p. 578 593, 2009.

[2] J. Blamey, E. J. Anthony, J. Wang, and P. S. Fennell, “The calcium looping cycle for large-scale CO_2 capture,” *Prog. Energ. Combust. Sci.*, vol. 36, no. 2, pp. 260–279, 2010.

[3] M. C. Romano, “Modeling the carbonator of a Ca-looping process for CO_2 capture from power plant flue gas,” *Chemical Engineering Science*, vol. 69, pp. 257 – 269, 2012.

[4] B. Arias, M. Diego, J. Abanades, M. Lorenzo, L. Diaz, D. Martinez, J. Alvarez, and A. Sanchez-Biezma, “Demonstration of steady state CO_2 capture in a 1.7 MWth calcium looping pilot,” *International Journal of Greenhouse Gas Control*, vol. 18, pp. 237–245, 2013.

[5] S. E. Edwards and V. Materic, “Calcium looping in solar power generation plants,” *Solar Energy*, vol. 86, no. 9, pp. 2494 – 2503, 2012.

[6] G. Flamant, D. Hernandez, C. Bonet, and J.-P. Traverse, “Experimental aspects of the thermochemical conversion of solar energy; decarbonation of $caco_3$,” *Solar Energy*, vol. 24, no. 4, pp. 385 – 395, 1980.

[7] J. M. Valverde, P. E. Sanchez-Jimenez, and L. A. Perez-Maqueda, “Calcium-looping for post-combustion CO_2 capture. on the adverse effect of sorbent regeneration under CO_2,” *Applied Energy*, vol. 126, pp. 161–171, 2014.

[8] J. M. Valverde, P. E. Sanchez-Jimenez, and L. A. Perez-Maqueda, “On the relevant influence of limestone crystallinity on CO_2 capture in the ca-looping technology at realistic calcination conditions,” *Environmental Science & Technology*, vol. 48, no. 16, pp. 9882–9889, 2014.

[9] E. P. Hyatt, I. B. Cutler, and M. E. Wadsworth, “Calcium carbonate decomposition in carbon dioxide atmosphere,” *Journal of the American Ceramic Society*, vol. 41, no. 2, pp. 70–74, 1958.

[10] D. Beruto, L. Barco, and A. W. Searcy, “CO_2-catalyzed surface area and porosity changes in high-surface-area CaO aggregates,” *Journal of the American Ceramic Society*, vol. 67, no. 7, pp. 512–516, 1984.

[11] E. L. Fuller and T. R. Yoos, “Surface properties of limestones and their activation products,” *Langmuir*, vol. 3, no. 5, pp. 753–760, 1987.

[12] J. M. Criado, M. Macias, and A. Macias-Machin, “Analysis of the system CaO-CO_2-H_2O for storage of solar thermal energy,” *Solar Energy*, vol. 49, pp. 83–86, 1992.

[13] J. M. Criado, M. Gonzalez, J. Malek, and A. Ortega, “The effect of the CO_2 pressure on the thermal decomposition kinetics of calcium carbonate,” *Thermochimica Acta*, vol. 254, pp. 121 – 127, 1995.

[14] J. Khinast, G. Krammer, C. Brunner, and G. Staudinger, “Decomposition of limestone: The influence of CO_2 and particle size on the reaction rate,” *Chemical Engineering Science*, vol. 51, no. 4, pp. 623–634, 1996.

[15] D. Dollimore, P. Tong, and K. S. Alexander, “The kinetic interpretation of the decomposition of calcium carbonate by use of relationships other than the arrhenius equation,” *Thermochimica Acta*, vol. 282–283, pp. 13 – 27, 1996.

[16] N. Koga and J. M. Criado, “The influence of mass transfer phenomena on the kinetic analysis for the thermal decomposition of calcium carbonate by constant rate thermal analysis (CRTA) under vacuum,” *Int. J. Chem. Kinet.*, vol. 30, pp. 737–744, 1998.

[17] F. Garcia-Labiano, A. Abad, L. de Diego, P. Gayan, and J. Adanez, “Calcination of calcium-based sorbents at pressure in a broad range of CO_2 concentrations,” *Chemical Engineering Science*, vol. 57, no. 13, pp. 2381 – 2393, 2002.

[18] D. Beruto, A. W. Searcy, and M. G. Kim, “Microstructure, kinetic, structure, thermodynamic analysis for calcite decomposition: free-surface and powder bed experiments,” *Thermochimica Acta*, vol. 424, no. 1 2, pp. 99 – 109, 2004.

[19] P. Michele, F. Loic, and S. Michel, “From the drawbacks of the arrhenius-f(α) rate equation towards a more general formalism and new models for the kinetic analysis of solid - gas reactions,” *Thermochimica Acta*, vol. 525, no. 1–2, pp. 93 – 102, 2011.

[20] I. Barin, *Thermochemicaldata of pure substances.* Weinheim: VCH., 1989.

[21] B. Stanmore and P. Gilot, “Review - calcination and carbonation of limestone during thermal cycling for CO_2 sequestration,” *Fuel Processing Technology*, vol. 86, no. 16, pp. 1707 – 1743, 2005.

[22] A. K. Galwey and M. E. Brown, “Application of the arrhenius equation to solid state kinetics: can this be justified?,” *Thermochimica Acta*, vol. 386, no. 1, pp. 91 – 98, 2002.

[23] A. Khawam and D. R. Flanagan, “Solid-state kinetic models: Basics and mathematical fundamentals,” *The Journal of Physical Chemistry B*, vol. 110, no. 35, pp. 17315 – 17328, 2006.

[24] D. Beruto and A. W. Searcy, “Use of the langmuir method for kinetic studies of decomposition reactions: calcite (caco3),” *J. Chem. Soc., Faraday Trans. 1*, vol. 70, pp. 2145–2153, 1974.

[25] C. N. R. Rao, S. R. Yoganarasimhan, and M. P. Lewis, “Exothermic reactions due to annealing of defects in oxide lattices: Study of the decomposition of carbonates,” *Canadian Journal of Chemistry*, vol. 38, no. 12, pp. 2359–2362, 1960.

[26] N. Rodriguez, M. Alonso, G. Grasa, and J. C. Abanades, “Heat requirements in a calciner of $CaCO_3$ integrated in a CO_2 capture system using CaO,” *Chemical Engineering Journal*, vol. 138, no. 1–3, pp. 148–154, 2008.

[27] L. M. Romeo, Y. Lara, P. Lisbona, and J. M. Escosa, “Optimizing make-up flow in a CO_2 capture system using CaO,” *Chemical Engineering Journal*, vol. 147, no. 2-3, pp. 252 – 258, 2009.

[28] A. Martinez, Y. Lara, P. Lisbona, and L. M. Romeo, “Operation of a cyclonic preheater in the Ca-looping for CO_2 capture,” *Environmental Science & Technology*, vol. 47, no. 19, pp. 11335–11341, 2013.

[29] I. Martinez, G. Grasa, R. Murillo, B. Arias, and J. Abanades, “Modelling the continuous calcination of $CaCO_3$ in a Ca-looping system,” *Chemical Engineering Journal*, vol. 215–216, pp. 174–181, 2013.

[30] J. Valverde, P. Sanchez-Jimenez, and L. Perez-Maqueda, “Ca-looping for postcombustion $\{CO_2\}$ capture: A comparative analysis on the performances of dolomite and limestone,” *Applied Energy*, vol. 138, no. 0, pp. 202 – 215, 2015.

[31] R. Besson, M. R. Vargas, and L. Favergeon, “CO_2 adsorption on calcium oxide: An atomic-scale simulation study,” *Surface Science*, vol. 606, no. 3 4, pp. 490 – 495, 2012.

[32] R. Besson and L. Favergeon, “Atomic - scale study of calcite nucleation in calcium oxide,” *The Journal of Physical Chemistry C*, vol. 117, no. 17, pp. 8813 – 8821, 2013.

[33] J. P. Allen, A. Marmier, and S. C. Parker, “Atomistic simulation of surface selectivity on carbonate formation at calcium and magnesium oxide surfaces,” *The Journal of Physical Chemistry C*, vol. 116, no. 24, pp. 13240 – 13251, 2012.

[34] M. Alonso, Y. Criado, J. Abanades, and G. Grasa, “Undesired effects in the determination of CO_2 carrying capacities of CaO during TG testing,” *Fuel*, vol. 127, pp. 52–61, 2014.

[35] G. Grasa, R. Murillo, M. Alonso, and J. C. Abanades, “Application of the random pore model to the carbonation cyclic reaction,” *AIChE J.*, vol. 55, no. 5, pp. 1246–1255, 2009.

[36] M. E. Brown, “The prout-tompkins rate equation in solid-state kinetics,” *Thermochimica Acta*, vol. 300, no. 1 - 2, pp. 93 – 106, 1997.

[37] S. Grazulis, A. Daskevic, A. Merkys, D. Chateigner, L. Lutterotti, M. Quiros, N. R. Serebryanaya, P. Moeck, R. T. Downs, and A. Le Bail, “Crystallography open database (COD): an open-access collection of crystal structures and platform for world-wide collaboration,” *Nucleic Acids Research*, vol. 40, no. D1, pp. D420–D427, 2012.

[38] K. M. Towe, “Ultrastructure of calcite decomposition in vacuo,” *Nature*, vol. 274, pp. 239 – 240, 1978.

[39] S. Dash, M. Kamruddin, P. Ajikumar, A. Tyagi, and B. Raj, “Nanocrystalline and metastable phase formation in vacuum thermal decomposition of calcium carbonate,” *Thermochimica Acta*, vol. 363, no. 1-2, pp. 129–135, 2000.

[40] N. Fatemi, R. Whitehead, D. Price, and D. Dollimore, “Some comments on the use of avrami-erofeev expressions and solid state decomposition rate constants,” *Thermochimica Acta*, vol. 104, no. 0, pp. 93 – 100, 1986.

[41] P. E. Sanchez-Jimenez, A. Perejon, J. M. Criado, M. J. Dianez, and L. A. Perez-Maqueda, “Kinetic model for thermal dehydrochlorination of poly(vinyl chloride),” *Polymer*, vol. 51, no. 17, pp. 3998 – 4007, 2010.

[42] P. Sun, J. R. Grace, C. J. Lim, and E. J. Anthony, “Determination of intrinsic rate constants of the CaO - CO_2 reaction,” *Chemical Engineering Science*, vol. 63, no. 1, pp. 47 – 56, 2008.

[43] A. Negi and S. Anand, *A Textbook of Physical Chemistry.* Wiley Eastern, 1985.

[44] M. Pijolat and M. Soustelle, “Experimental tests to validate the rate-limiting step assumption used in the kinetic analysis of solid–state reactions,” *Thermochimica Acta*, vol. 478, no. 1–2, pp. 34 – 40, 2008.

[45] A. M. Kierzkowska, R. Pacciani, and C. R. Müller, “CaO-based CO_2 sorbents: From fundamentals to the development of new, highly effective materials,” *ChemSusChem*, vol. 6, no. 7,

pp. 1130–1148, 2013.

[46] A. W. Searcy and D. Beruto, “Kinetics of endothermic decomposition reactions. i. steady-state chemical steps,” *The Journal of Physical Chemistry*, vol. 80, no. 4, pp. 425–429, 1976.

[47] D. Beruto, A. W. Searcy, and M. G. Kim, “Calcium oxides of high reactivity,” *Nature*, vol. 5574, pp. 221 – 222, 1976.

[48] J. Rouquerol, “Critical examination of several problems typically found in the kinetic study of thermal decomposition under vacuum,” *Journal of thermal analysis*, vol. 5, no. 2–3, pp. 203–216, 1973.

[49] H.-Y. Xie and D. Geldart, “Fluidization of FCC powders in the bubble-free regime: effect types of gases and temperature,” *Powder Technol.*, vol. 82, pp. 269 – 277, 1995.

[50] R. H. Borgwardt, “Sintering of nascent calcium oxide,” *Chem. Eng. Sci.*, vol. 44, no. 1, pp. 53–60, 1989.

[51] R. H. Borgwardt, “Calcium oxide sintering in atmospheres containing water and carbon dioxide,” *Industrial & Engineering Chemistry Research*, vol. 28, no. 4, pp. 493 – 500, 1989.

[52] J. Valverde, J. M. P. Ebri, and M. A. S. Quintanilla, “Acoustic streaming enhances the multicyclic CO_2 capture of natural limestone at Ca-looping conditions,” *Environmental Science & Technology*, vol. 47, no. 16, p. 9538 9544, 2013.

[53] R. M. German and Z. A. Munir, “Surface area reduction during isothermal sintering,” *Journal of the American Ceramic Society*, vol. 59, no. 9 - 10, p. 379 383, 1976.

[54] D. Dollimore, “Thermodynamic, kinetic and surface texture factors in the production of active solids by thermal decomposition,” *Journal of thermal analysis*, vol. 38, no. 1-2, pp. 111 – 130, 1992.

[55] C. R. Milne, G. D. Silcox, D. W. Pershing, and D. A. Kirchgessner, “Calcination and sintering models for application to high-temperature, short-time sulfation of calcium-based sorbents,” *Industrial & Engineering Chemistry Research*, vol. 29, no. 2, pp. 139–149, 1990.

[56] A. B. Fuertes, D. Alvarez, F. Rubiera, J. J. Pis, and G. Marban, “Surface area and pore size changes during sintering of calcium oxide particles,” *Chemical Engineering Communications*, vol. 109, no. 1, pp. 73 – 88, 1991.

[57] C. H. Bartholomew, “Sintering kinetics of supported metals: new perspectives from a unifying GPLE treatment,” *Applied Catalysis A: General*, vol. 107, no. 1, pp. 1 – 57, 1993.

[58] G. Silcox, J. Kramlich, and D. Pershing, “A mathematical model for the flash calcination of dispersed $CaCO_3$ and $Ca(OH)_2$ particles,” *Ind. Eng. Chem. Res.*, vol. 28, p. 155 160, 1989.

[59] G. S. Grasa and J. C. Abanades, “CO_2 capture capacity of CaO in long series of carbonation/calcination cycles,” *Ind. Eng. Chem. Res.*, vol. 45, no. 26, pp. 8846–8851, 2006.

[60] J. M. Valverde, P. E. Sanchez Jimenez, A. Perejon, and L. A. Perez-Maqueda, “CO_2 multicyclic capture of pretreated/doped CaO in the Ca – looping process. Theory and experiments,” *Phys. Chem. Chem. Phys.*, vol. 15, pp. 11775 – 11793, 2013.

[61] J. Ewing, D. Beruto, and A. W. Searcy, “The nature of CaO produced by calcite powder decomposition in vacuum and in CO_2,” *Journal of the American Ceramic Society*, vol. 62, no. 11-12, pp. 580–584, 1979.

[62] S. Stendardo, L. Andersen, and C. Herce, “Self-activation and effect of regeneration conditions in CO_2 carbonate looping with CaO Ca_{12} Al_{14} O_{33} sorbent,” *Chemical Engineering Journal*, vol. 220, pp. 383 – 394, 2013.

[63] R. Barker, “Reversibility of the reaction $CaCO_3$ =CaO+CO_2,” *J. Appl. Chem. Biotechnol.*, vol. 23, pp. 733 – 742, 1973.

[64] S. K. Bhatia and D. D. Perlmutter, “Effect of the product layer on the kinetics of the CO_2-lime reaction,” *AIChE Journal*, vol. 29, no. 1, pp. 79–86, 1983.

[65] Z. Sun, S. Luo, P. Qi, and L.-S. Fan, “Ionic diffusion through calcite ($CaCO_3$) layer during the reaction of cao and CO_2,” *Chemical Engineering Science*, vol. 81, pp. 164 – 168, 2012.

[66] J. M. Valverde, “A model on the CaO multicyclic conversion in the Ca-looping process,” *Chemical Engineering Journal*, vol. 228, pp. 1195–1206, 2013.

[67] D. Alvarez and J. C. Abanades, “Pore-size and shape effects on the recarbonation performance of calcium oxide submitted to repeated calcination/recarbonation cycles,” *Energy and Fuels*, vol. 19, pp. 270–278, 2005.

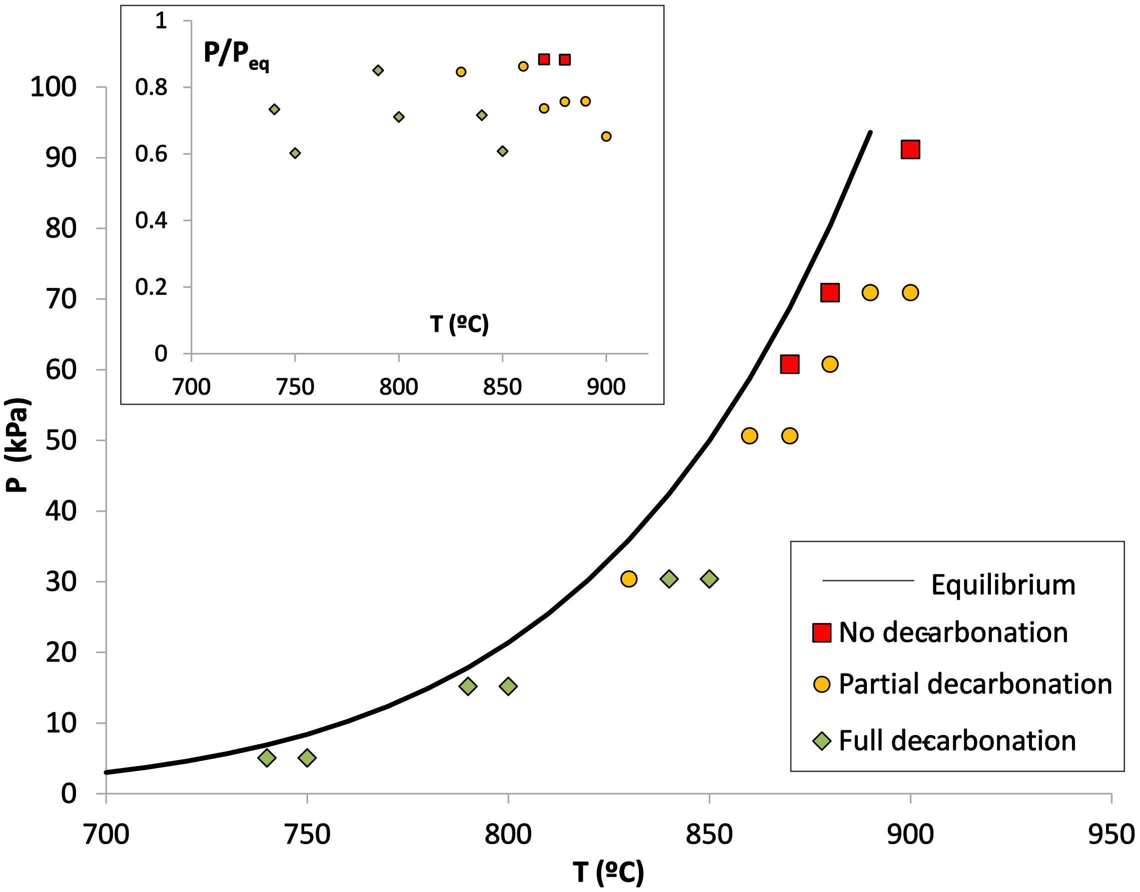

FIG. 1: CO_2 partial pressure P and temperature in the calcination tests carried out. It is indicated whether full decarbonation was achieved in the 1 h calcination period or partial decarbonation or no decarbonation at all (in-situ XRD analysis). The solid line represents the CO_2 equilibrium pressure as a function of temperature. The inset shows the ratio of CO_2 partial pressure to equilibrium pressure as a function of the calcination temperature.

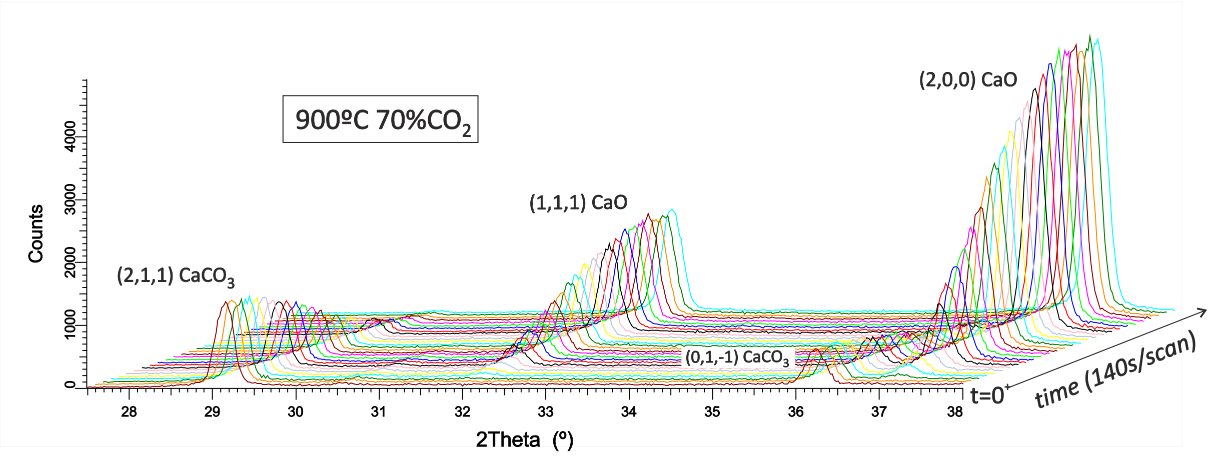

FIG. 2: Diffractograms obtained from in-situ XRD analysis during calcination at 900°C under 70% CO_2.

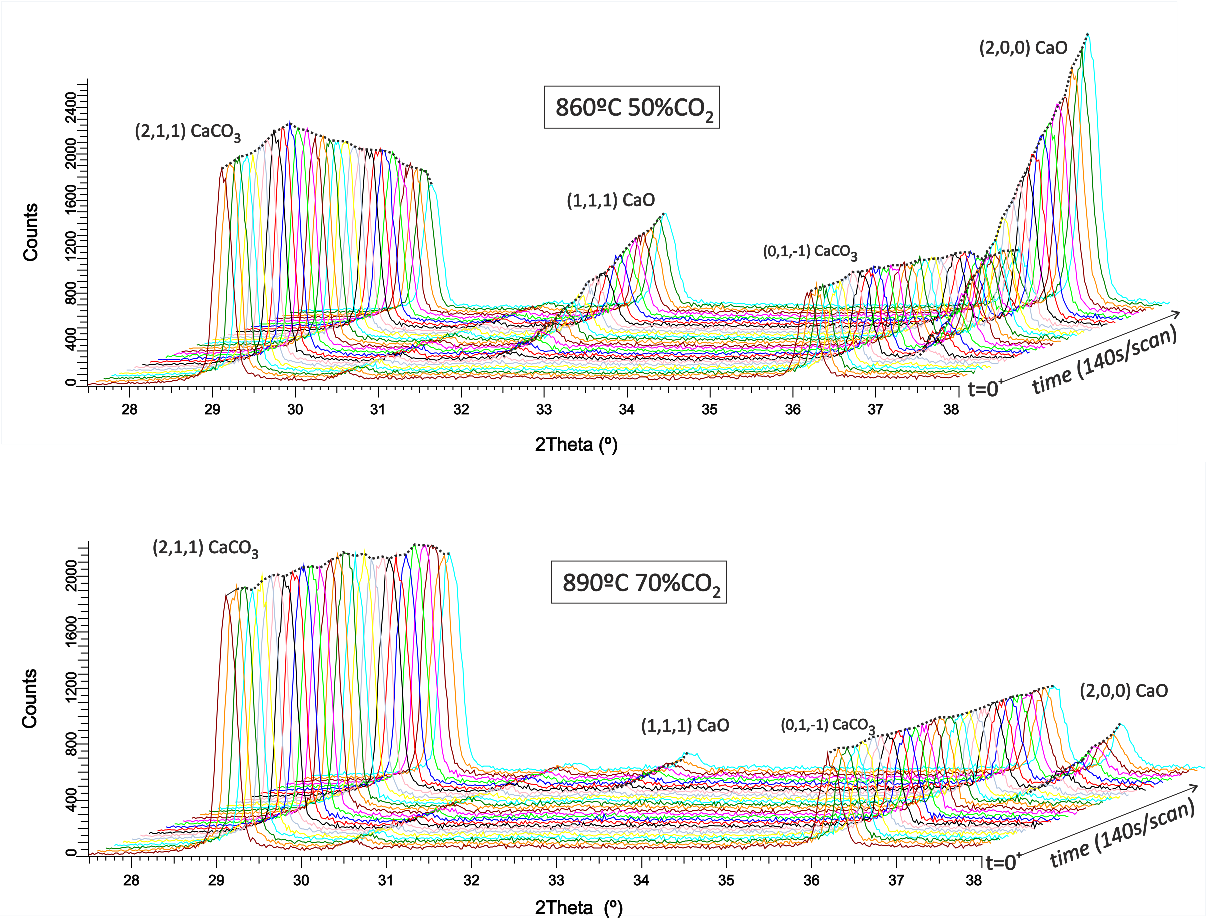

FIG. 3: Diffractograms obtained from in-situ XRD analysis during calcination at the conditions indicated.

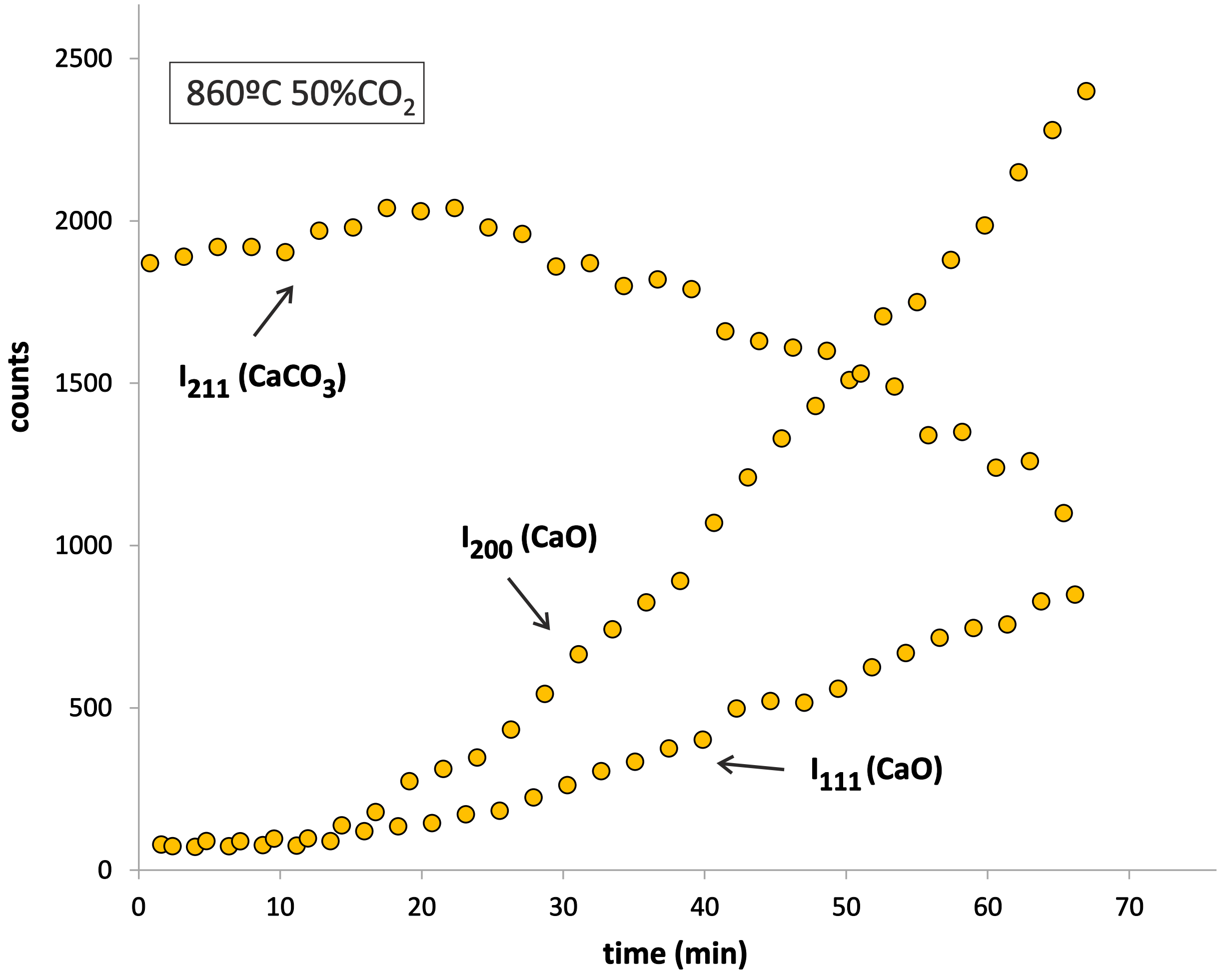

FIG. 4: Intensities at the indicated Bragg reflection peaks as a function of calcination time at 860°C/50%CO_2 obtained from in-situ XRD analysis.

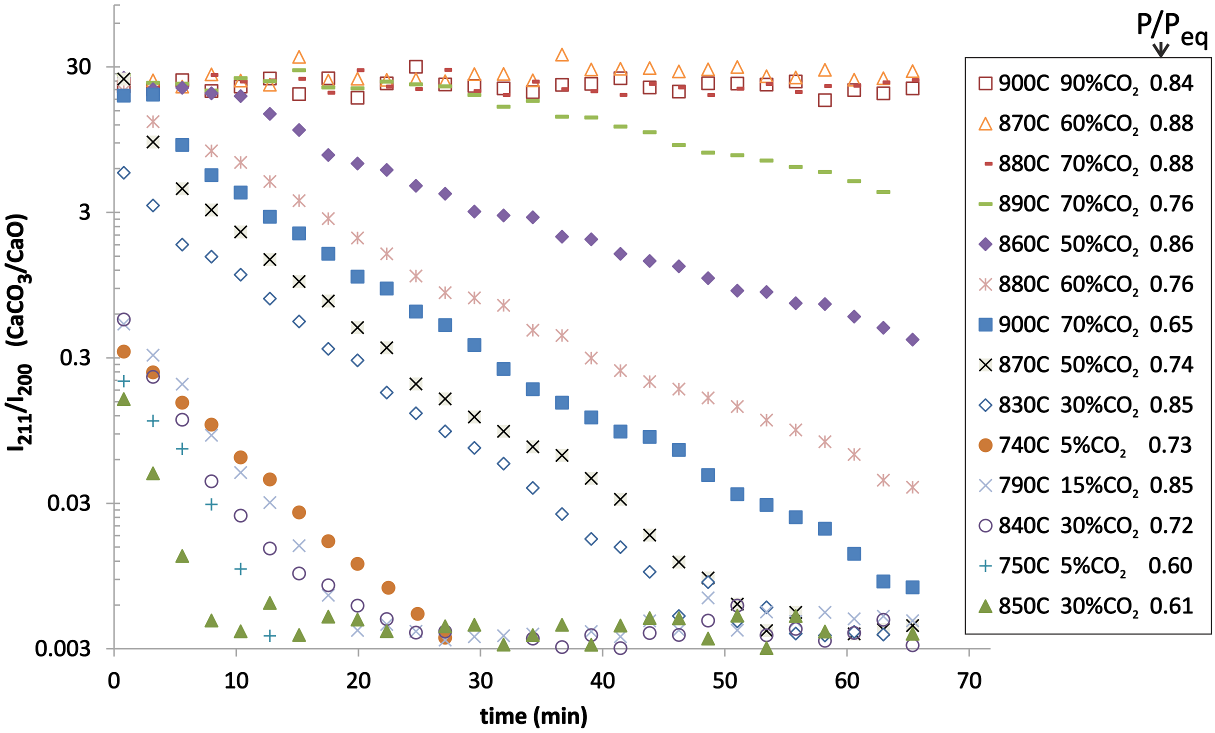

FIG. 5: Ratio of intensity at $CaCO_3$ (211) main reflection peak position ($2\theta \simeq 29.2°$) to intensity at CaO (200) main peak position ($2\theta \simeq 37.1°$) during calcination at diverse temperatures and CO_2 vol.% (as indicated) obtained during in-situ XRD analysis. Note the vertical log scale.

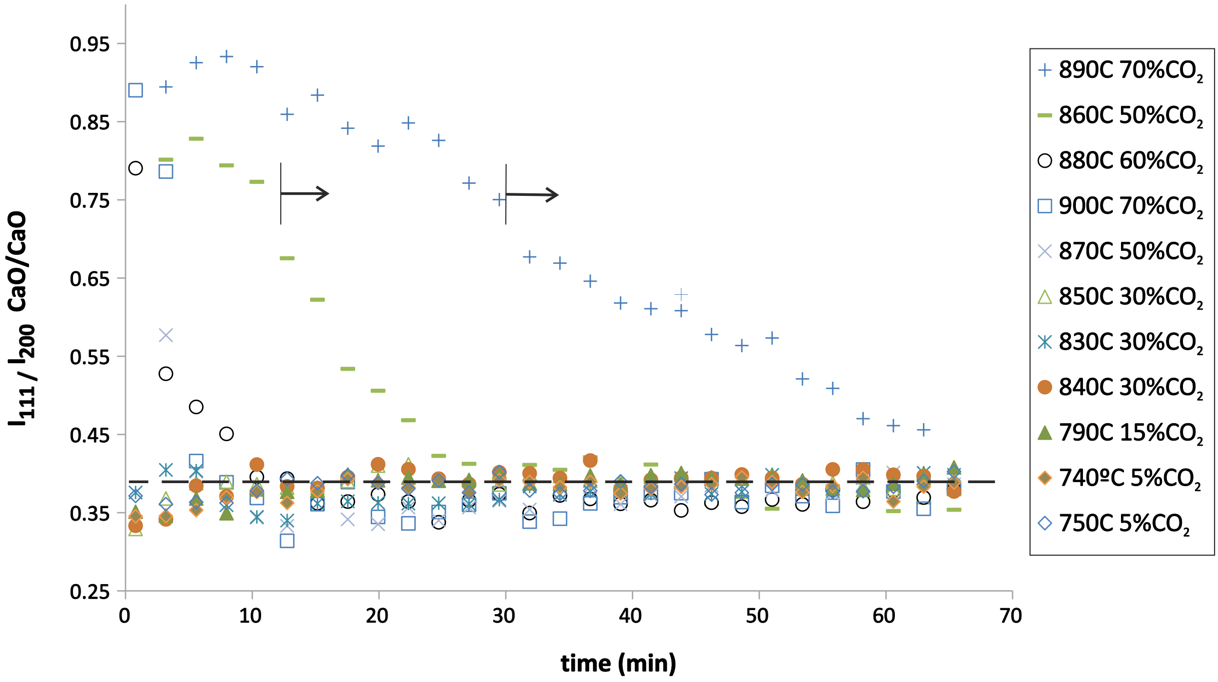

FIG. 6: Ratio of intensity at CaO (111) reflection peak position ($2\theta \simeq 32°$) to intensity at CaO (200) peak position ($2\theta \simeq 37.1°$) during calcination at diverse temperatures and CO_2 vol.% (as indicated) obtained by in-situ XRD analysis. The horizontal arrows indicate the initiation of decarbonation after an induction period as inferred from Fig. 5. The horizontal dashed line indicates the intensities ratio I_{111}/I_{200} given by the CaO (lime) reference pattern ($I_{111}/I_{200} = 0.389$) available from Crystallography Open Database (COD) [37].

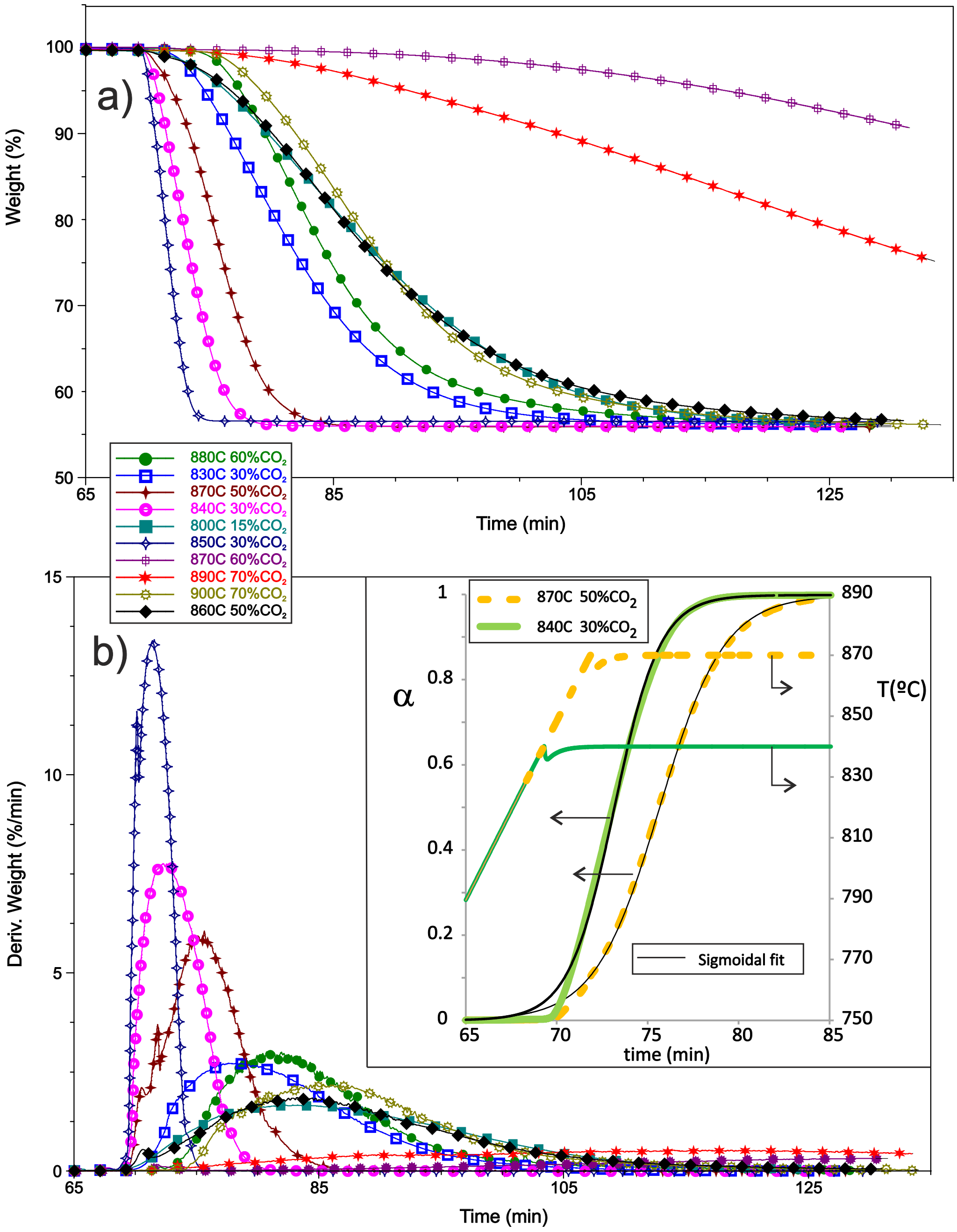

FIG. 7: Time evolution of sample weight (wt.%) (a) and weight % time derivative (b) measured in the TGA tests during calcination at diverse temperatures and CO_2 vol.% (as indicated). The inset of b) shows for two examples the time evolution of $CaCO_3$ conversion derived from the thermogram ($\alpha = (100/44)\Delta wt/wt_0$) and temperature in the tests. The solid lines represent best sigmoidal fit curves ($\alpha(t) \simeq 1/(1+\exp(-\beta(t-t_0)))$)

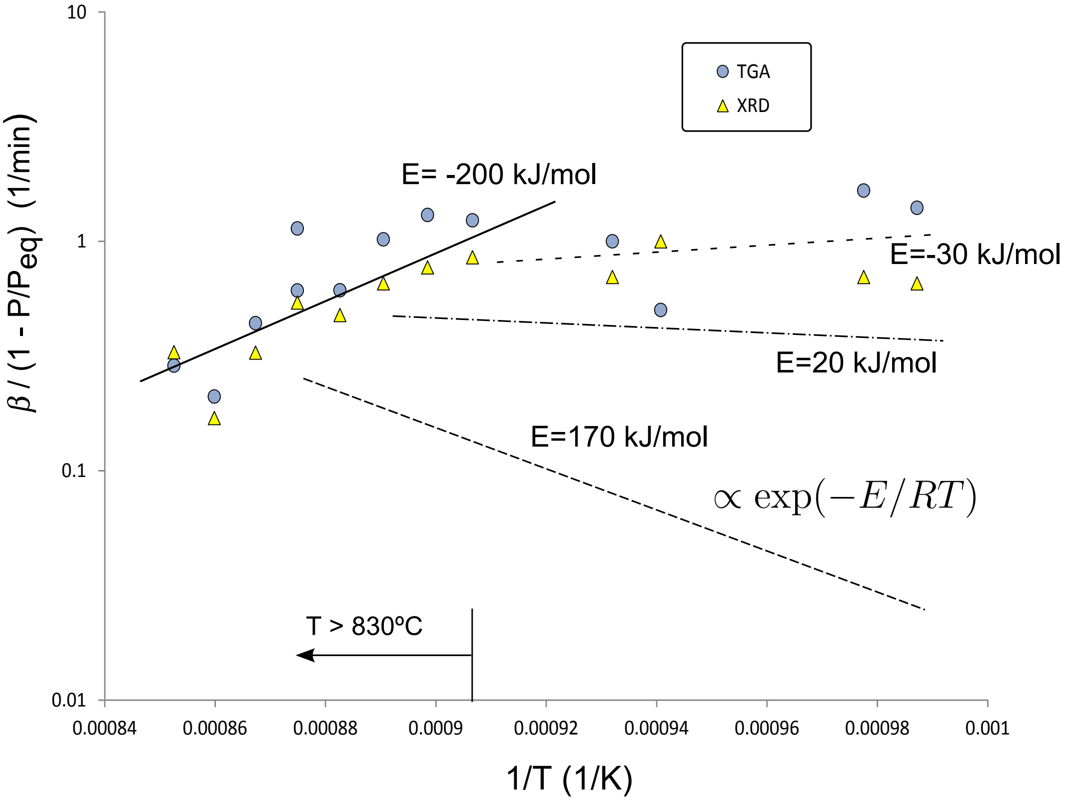

FIG. 8: Reaction rate divided by $(1 - P/P_{eq})$ as a function of $1/T(K)$ obtained from calcination tests by means of TGA and in-situ XRD analysis as indicated and predicted by the laws $r/(1 - P/P_{eq}) \propto \exp(-E/RT)$.

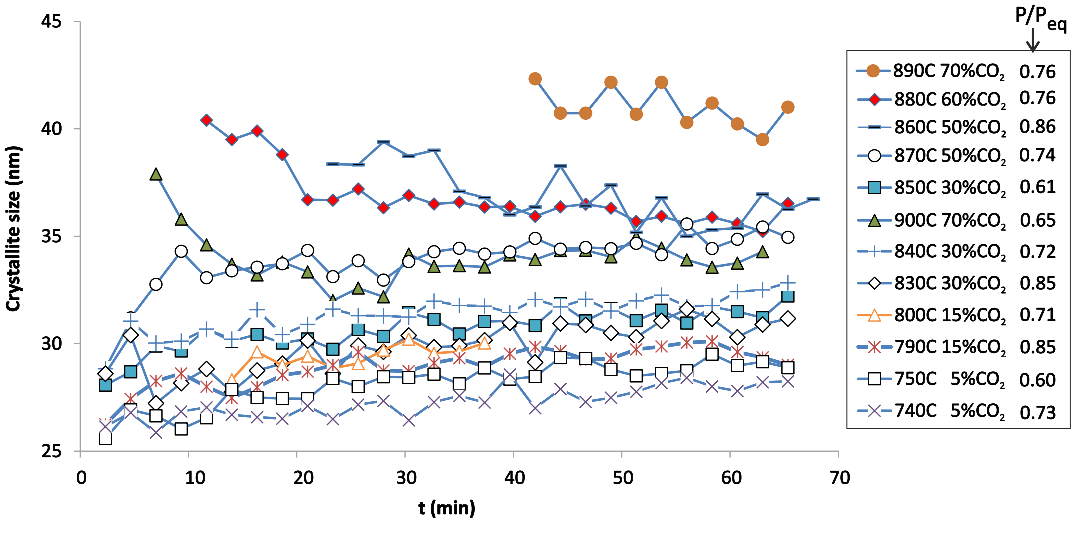

FIG. 9: CaO crystallite size (L_c) as a function of calcination time determined by CaO (200) peak broadening analysis from the in-situ XRD tests.

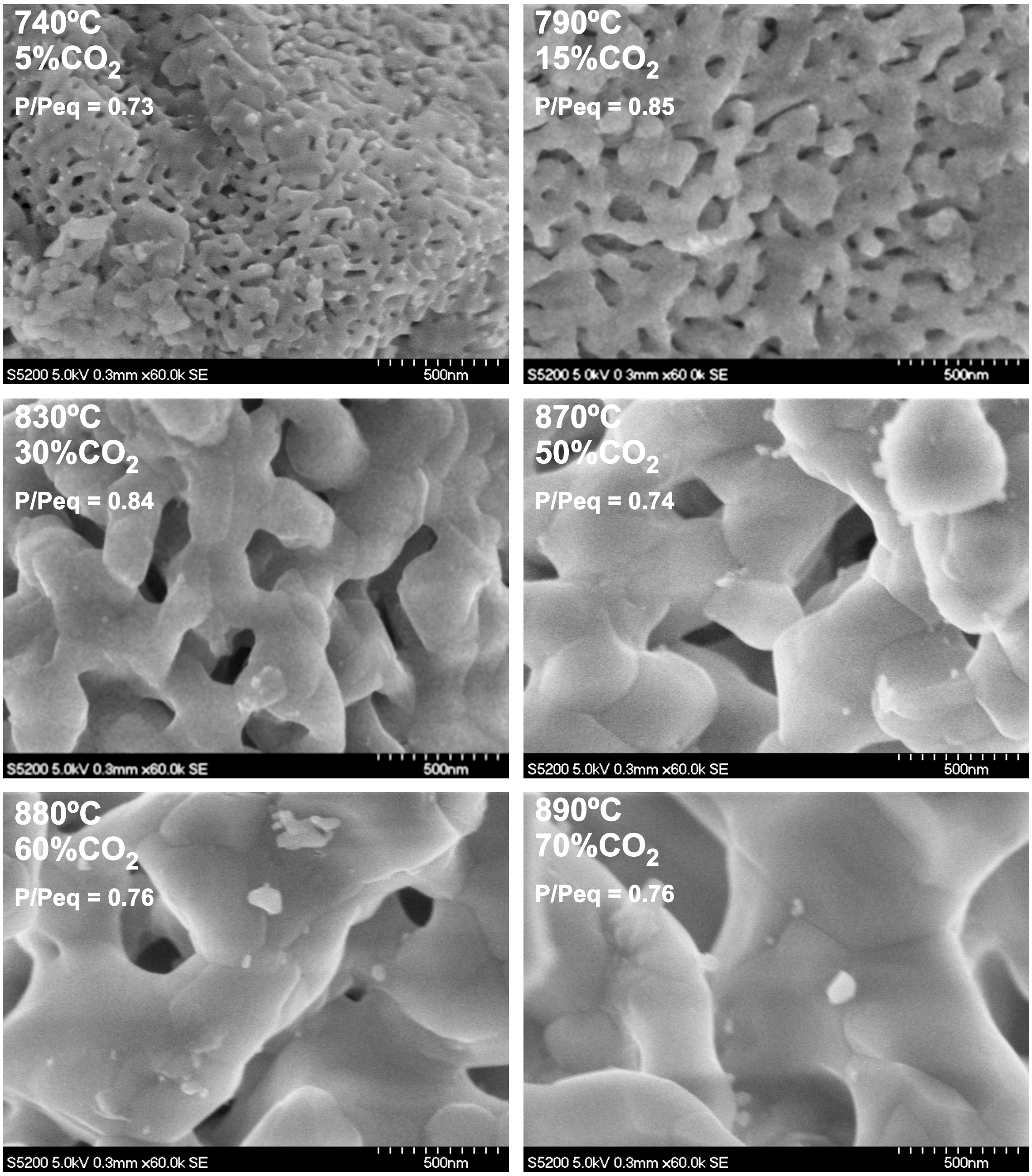

FIG. 10: Representative SEM images of samples calcined in the XRD chamber at diverse conditions of temperature and CO_2 concentration. Values of the ratio of CO_2 partial pressure to equilibrium partial pressure are indicated.

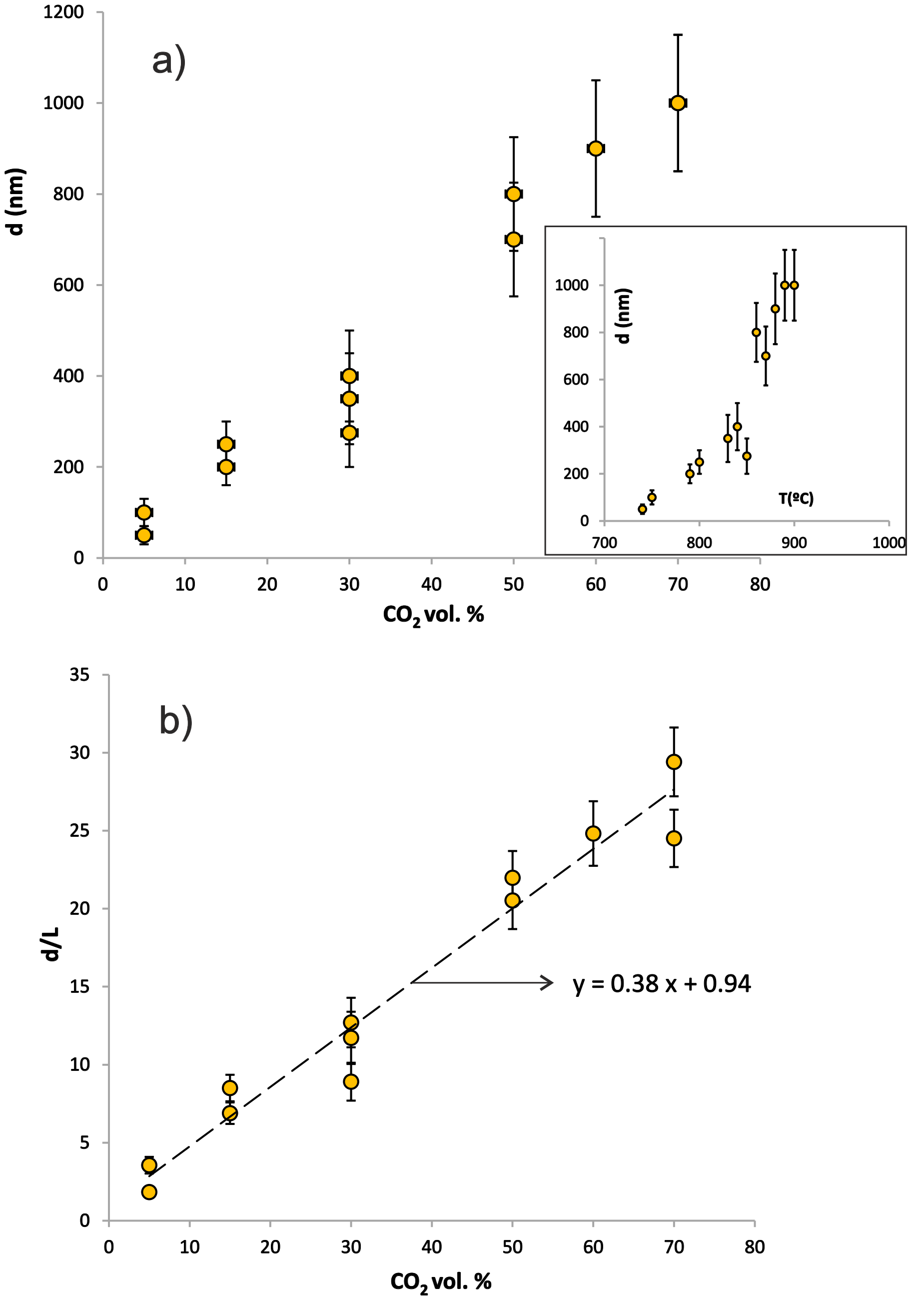

FIG. 11: a) CaO grain size d obtained from SEM images of samples calcined in the XRD chamber as a function of the CO$_2$ vol.% in the calcination atmosphere. The inset shows d versus the calcination temperature. b) Ratio of grain size to average crystallite size. The dashed line represents the best fit linear law ($d/L_c \simeq 1 + 0.4\,[\text{CO}_2 \text{ vol.\%}]$).

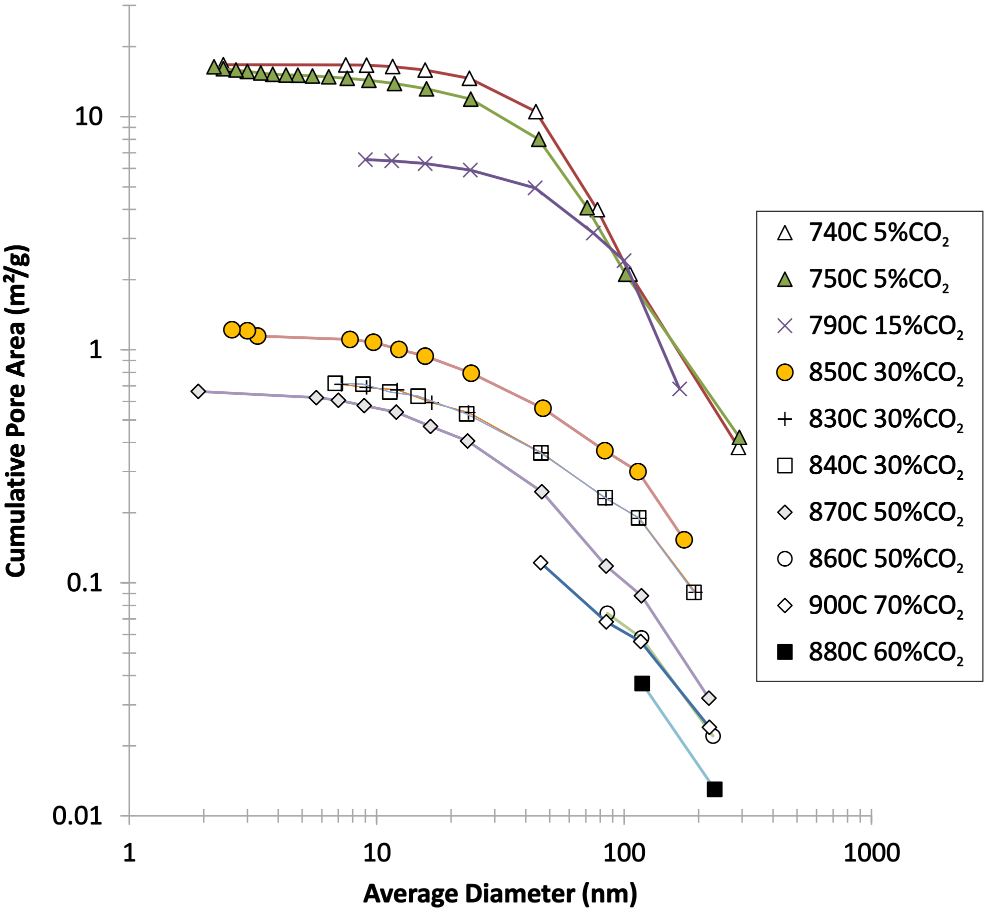

FIG. 12: Cumulative pore area distributions obtained by N_2 physisorption (77 K) analysis on the samples calcined in the XRD chamber.

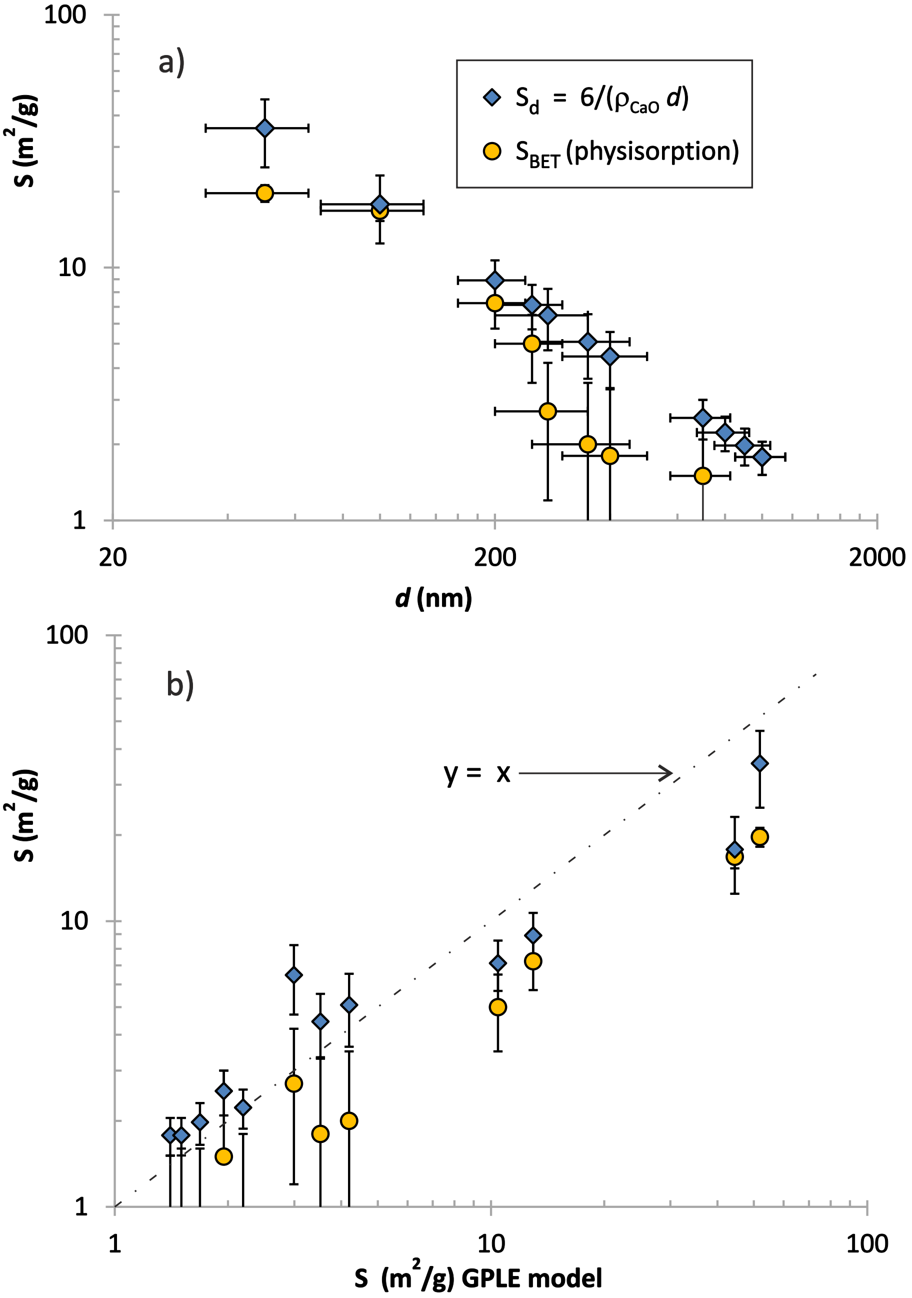

FIG. 13: a) Surface area of the samples calcined in the XRD chamber as a function of grain size d (obtained from SEM analysis, Fig. 11). Surface area values are shown as measured from N_2 physisorption analysis (S_{BET}) and estimated from grain size S_d . b) S_{BET} and S_d versus predicted values from equation Eq. 34 using $k = 10K_s$ (Eq. 32).

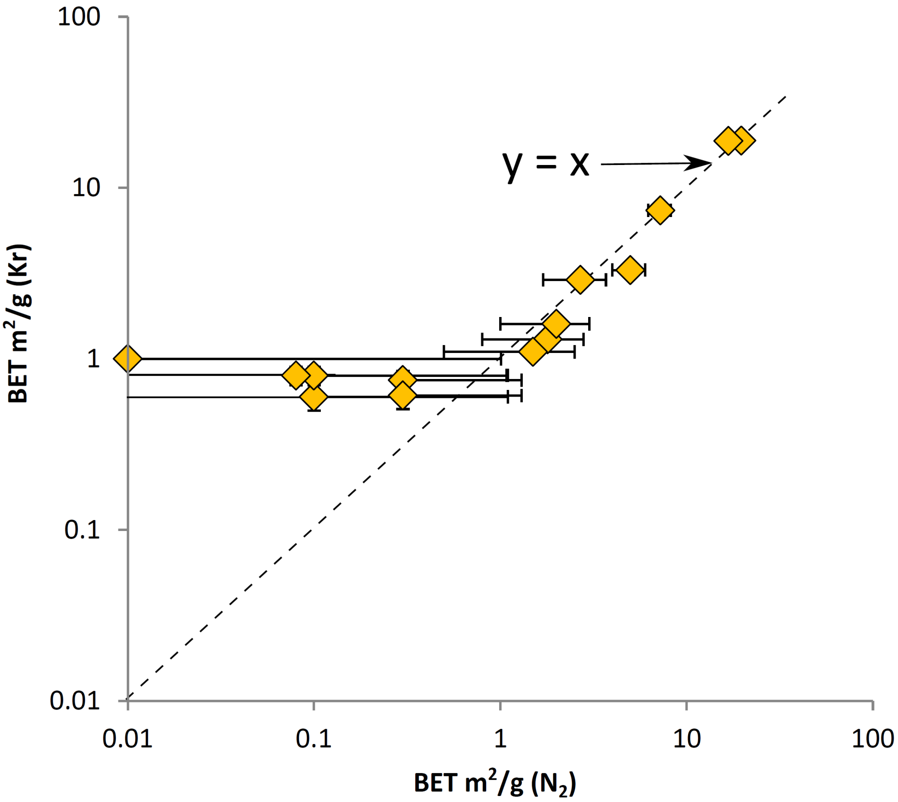

FIG. 14: BET surface area as measured from physisorption analysis using Kr (vertical axis) and N_2 (horizontal axis).

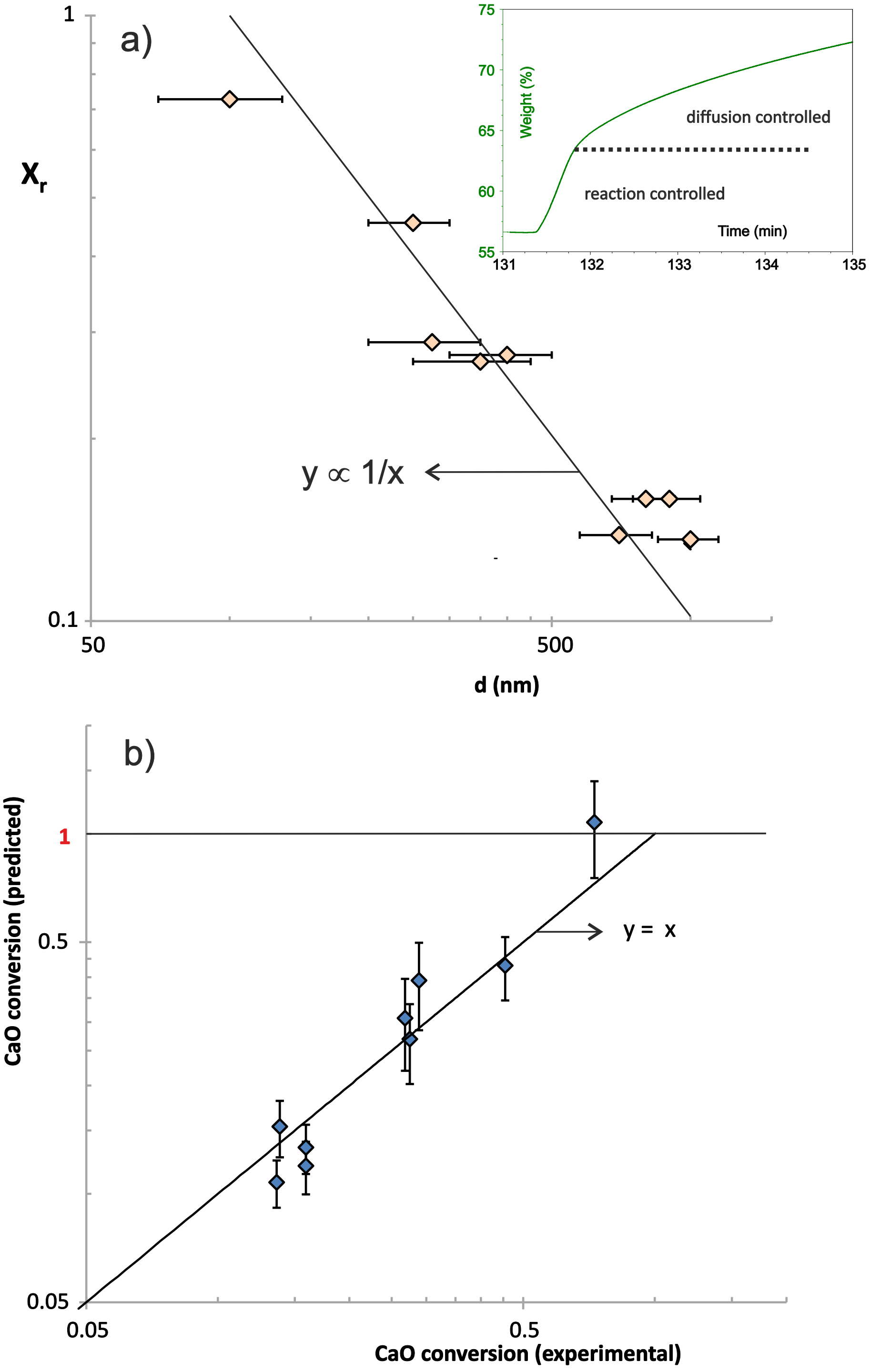

FIG. 15: a) CaO conversion in the reaction controlled phase measured in the TGA tests (at 650°C/15%CO_2 just after calcination) as a function of grain size d derived from SEM analysis (Fig. 11). The inset shows the time evolution of sample wt% during carbonation of CaO derived from calcination in-situ (860°C/50%CO_2) illustrating the border between the reaction controlled and diffusion controlled carbonation phases. b) CaO conversion in the reaction controlled phase measured versus predicted from Eq. 35 using the surface area estimated from the grain size S_d and $h = 40$ nm.